

Paleoceanography and Paleoclimatology

RESEARCH ARTICLE

10.1029/2019PA003845

Key Points:

- A coupled climate simulation of the early Eocene shows a single intense overturning cell originating in the Southern Ocean
- Lagrangian analysis of this paleo-Antarctic Bottom Water reveals a major route to the surface mixed layer, with implications for carbon cycle
- This upwelling mainly occurs in equatorial and tropical regions, in relation with the spatial pattern of the wind-driven Ekman pumping

Supporting Information:

- Supporting Information S1

Correspondence to:

Y. Zhang,
yurui.zhang@univ-brest.fr

Citation:

Zhang, Y., Grima, N., & Huck, T. (2021). Fates of paleo-Antarctic Bottom Water during the early Eocene: Based on a Lagrangian analysis of IPSL-CM5A2 climate model simulations. *Paleoceanography and Paleoclimatology*, 36, e2019PA003845. <https://doi.org/10.1029/2019PA003845>

Received 27 DEC 2019

Accepted 1 DEC 2020

Accepted article online 14 DEC 2020

Fates of Paleo-Antarctic Bottom Water During the Early Eocene: Based on a Lagrangian Analysis of IPSL-CM5A2 Climate Model Simulations

Yurui Zhang^{1,2} , Nicolas Grima¹ , and Thierry Huck¹ 

¹Univ Brest, CNRS, IRD, Ifremer, Laboratoire d'Océanographie Physique et Spatiale (LOPS), IUEM, Brest, France,

²College of Ocean and Earth Sciences, Xiamen University, Xiamen, China

Abstract Both deepwater formation and the obduction processes converting dense deep water to lighter surface water are the engine for the global meridional overturning circulation (MOC). Their spatio-temporal variations effectively modify the ocean circulation and related carbon cycle, which affects climate evolution throughout geological time. Using early-Eocene bathymetry and enhanced atmospheric CO₂ concentration, the IPSL-CM5A2 climate model has simulated a well-ventilated Southern Ocean associated with a strong anticlockwise MOC. To trace the fates of these paleo-Antarctic Bottom Water (paleo-AABW), we conducted Lagrangian analyses using these IPSL-CM5A2 model results and tracking virtual particles released at the lower limb of the MOC, defined as an initial section at 60°S below 1,900 m depth. Diagnostic analysis of these particles trajectories reveals that most paleo-AABW circulates back to the Southern Ocean through either the initial section (43%) or the section above (31%), the remaining (>25%) crossing the base of the mixed layer mostly in tropical regions (up to half). The majority of water parcels ending in the mixed layer experience negative density transformations, intensified in the upper 500 m and mostly occurring in tropical upwelling regions, with a spatial pattern consistent with the wind-driven Ekman pumping, largely determined by the Eocene wind stress and continental geometry. In the same way as present-day North Atlantic Deep Water upwells in the Southern Ocean, our results suggest that the strong tropical and equatorial upwelling during the Eocene provides an efficient pathway from the abyss to the surface, but at much higher temperature, with potential implications for the oceanic carbon cycle.

1. Introduction

The formation of dense deep and/or bottom water masses and their conversion into light surface water act as an engine for the global meridional overturning circulation (MOC) and characterizes the interactions between the surface and abyssal (interior) ocean (e.g., Bullister et al., 2013; Kuhlbrodt et al., 2007). Wind-driven upwelling in the Southern Ocean in present-day conditions provides a pathway for North Atlantic Deep Water (NADW) toward the thermocline and closes the Atlantic Meridional Overturning Circulation (AMOC), forming the quasi-adiabatic pole-to-pole overturning circulation (Anderson et al., 2009; Marshall & Speer, 2012; Wolfe & Cessi, 2011). Spatio-temporal variations in deepwater formation and its obduction, such as intensity, location and timescale, effectively modify the global ocean circulation that shapes the global climate on multiple timescales (Burke & Robinson, 2012; Kuhlbrodt et al., 2007; Nof, 2000; Srokosz et al., 2012; Toggweiler & Samuels, 1995). Ocean circulation carries a huge amount of heat and thus largely alters global heat distribution (Ganachaud & Wunsch, 2000; Macdonald & Wunsch, 1996; Trenberth & Caron, 2001). Meanwhile, long-term variations (on a scale of thousands to millions of years) in deepwater dynamics modify the carbon storage capacity of the deep ocean and adjust the carbon exchange between the deep-ocean carbon inventory and atmosphere, which plays an important role in the evolution of the Earth's climate (Anderson et al., 2009; Broecker & Barker, 2007). For example, the variations in Southern Ocean upwelling, associated with related physico-chemical and biogeochemical processes, have been found to regulate fluctuations of atmospheric CO₂ and climate evolution across the late Pleistocene glacial cycles (Anderson et al., 2009; Burke & Robinson, 2012; Martínez-Botí et al., 2015; Sigman & Boyle, 2000; Watson & Naveira Garabato, 2006). Strengthened upwelling during deglaciations increases the exposure rate of the deep ocean, which can trigger a series of physico-chemical (e.g., solubility of seawater) and biogeochemical responses (e.g., nutrient availability and export production) and enhance

CO₂ release into the atmosphere. In contrast, weakened upwelling contributes to decreased carbon release from the abyssal ocean, thereby facilitating the sequestration of atmospheric carbon (Anderson et al., 2009; Burke & Robinson, 2012; Martínez-Botí et al., 2015; Watson & Naveira Garabato, 2006). Understanding these changing interactions between the abyssal ocean's carbon reservoir and surface ocean is thus of utmost importance for decoding climate evolution on various timescales.

Paleoceanographic data has shown that interactions between the deep and surface ocean have gone through multiple-scale changes over geological history in response to a variety of forcings (e.g., Ferreira et al., 2018). Geological records indicate that the early Eocene was characterized by an extremely warm climate (5–8°C warmer than the present day) and very active global carbon cycle with enhanced exchanges among different components of the Earth system, (Cramer et al., 2011; Dunkley Jones et al., 2013; Foster et al., 2017; Hollis et al., 2019; Pearson & Palmer, 2000; Tripathi et al., 2003). Numerous CO₂-proxy data report high atmospheric CO₂ concentrations during the early Eocene (Breecker et al., 2010; Foster et al., 2017; Pagani et al., 1999; Pearson & Palmer, 2000; Tripathi et al., 2003), which is undoubtedly a critical factor causing this warm climate, if not the primary one. Although this enhanced atmospheric CO₂ level may partially result from carbon input from the biosphere—such as in a response to irreversible degradation of biomass as tropical ecosystems crossed a thermal threshold of 35°C for vegetation (Huber, 2008) or as high-latitude permafrosts experienced oxidation of soil organic carbon (DeConto et al., 2012; Kurtz et al., 2003)—the carbon cycle was definitely influenced by the deep-ocean carbon reserves during the early Eocene. The deep ocean is a huge carbon reservoir, and its reorganization during the early Eocene left an imprint in the global carbon cycle (e.g., John et al., 2013, 2014). A plausible mechanism for this carbon perturbation remains elusive yet, leaving our understanding of Eocene Earth system evolution incomplete.

Considering the crucial influence of the deep-ocean carbon reservoir on global carbon cycle during the late Pleistocene glacial cycles (Anderson et al., 2009; Burke & Robinson, 2012), carbon exchanges between the deep ocean and the surface may hold the key for understanding the early-Eocene climate system (John et al., 2013, 2014). Global acidification of the surface ocean and widespread dissolution of deep-sea carbonates during the early Eocene also suggest a large-scale reorganization of the oceanic carbon cycle system (John et al., 2013, 2014). Such large-scale changes of carbon-related processes in the ocean may alter the carbon exchange between the abyssal ocean carbon reservoir and the surface ocean, which likely link to a different early-Eocene meridional ocean circulation. Within the framework of the Deep-Time Model Inter-comparison Project (DeepMIP; Lunt et al., 2017), including 840 ppm atmospheric CO₂ (three times the pre-industrial (PI) levels) and realistic Eocene bathymetry and other boundary conditions (e.g., no Antarctic ice sheet), the IPSL-CM5A2 model has simulated a vigorous MOC originating in the Southern Ocean, as discussed in Zhang et al. (2020). This MOC is sustained by deepwater formation occurring at high latitudes of the Southern Ocean, where denser water sinks into the depths and fills the whole ocean basins. Given this very different oceanic circulation and specificity of the early Eocene (regarding the climatic environment and the global carbon cycle), it is of utmost interest to understand how these dense waters formed by deep convection are transformed into light water returning to the surface thermocline, for example, at what rate they are transformed and where this process occurs.

One frequently used way to understand paleo-oceanic circulation for relatively recent periods is to compare it with present-day conditions and to analyze circulation anomalies relative to the PI condition. However, the fact that both bathymetry and MOC during the deep geological time of Eocene (cf. Zhang et al., 2020) are so different from those of the present day hinders this direct comparison. With such a different MOC structure and in the absence of an Antarctic Circumpolar Current, one can expect different thermodynamic processes and physical mechanisms to close the global ocean circulation and associated transformation of deep water into light surface water during the early Eocene, which are still unknown yet. Through the diagnosis of virtual particle trajectories, Lagrangian analysis provides an accessible way to investigate the movement of dense deep water and their density transformations, and to diagnose their interactions with the surface thermocline in given three-dimensional, time-evolving velocity fields (e.g., Blanke et al., 2002; Tamsitt et al., 2017, 2018). In this study, we applied such a Lagrangian analysis to investigate the fate of the paleo-Antarctic Bottom Water (hereafter referred to as paleo-AABW, for both bottom and deep waters in the absence of other deepwater mass). Using the IPSL-CM5A2 climate model results for the early Eocene, this analysis allows to map the 3-D circulation of the paleo-AABW, and in particular how it

upwells back toward the upper ocean. In order to better understand the closure regime of the Eocene MOC in the model simulation, we specifically set out to (1) map the general pathways of the paleo-AABW circulation and upwelling and (2) diagnose the underlying dynamical and thermodynamic processes behind this upwelling and associated density transformations. In addition, the results of this analysis can also extend our knowledge on the closure of the MOC in a context that is quite different than the present day, especially in the absence of a quasi-adiabatic pole-to-pole overturning circulation regime. We first introduce the paleo-climate simulation that is used, then the details of the Lagrangian analysis (section 2). Sections 3 and 4 present the Lagrangian results, and their discussion on and implication on Eocene global carbon cycle, respectively. Summary and conclusions are given in section 5.

2. Methods

2.1. The Early-Eocene Simulation and Its Evaluation

The early-Eocene simulation used in this study has been discussed in Zhang et al. (2020) with detailed information on boundary condition and on simulation setup, so we only provide a brief summary of the simulation hereafter. The simulation was performed with the IPSL-CM5A2 (Institut Pierre Simon Laplace) climate model and set up with the boundary conditions reconstructed for the early Eocene (~55 Ma), following the DeepMIP (Deep-Time Model Inter-comparison Project) protocol (Lunt et al., 2017). The IPSL-CM5A2 is a new version of IPSL-CM5A: an Earth system climate model comprising the LMDz atmospheric model, and the NEMO (Nucleus for European Modeling of the Ocean) ocean model with a spatial resolution of ~2°, coupled to the LIM2 dynamical sea ice model through the OASIS coupler (Dufresne et al., 2013; Hourdin et al., 2013; Sepulchre et al., 2020). The NEMO ocean model has 31 vertical levels with a finer resolution near the surface (10 m) than in the abyss (~500 m), and partial steps were used for the level directly above seafloor to better represent the bathymetry. The previous version IPSL-CM5A has been extensively used in various contexts, such as the Last Glacial Maximum, the mid-Holocene (Kageyama et al., 2013), and the Pliocene (Contoux et al., 2013; Tan et al., 2017, 2020). The new version IPSL-CM5A2, recently developed by Sepulchre et al. (2020) for faster computation, is dedicated to the analysis of deep time history of the Earth system. For instance, this new version model has been used to simulated Pliocene (Tan et al., 2018, 2020) and Eocene climate (Ladant et al., 2014; Zhang et al., 2020), in which plate tectonic forces, such as changes in continents geography and seafloor bathymetry, are permitted. The boundary conditions of this early-Eocene simulation include an atmospheric CO₂ concentration of three times that of PI levels (840 ppm), bathymetry and topography reconstructed for the early Eocene (Herold et al., 2014; see supporting information Figure S1), and prescribed tidally induced mixing (Green & Huber, 2013). The simulation was initialized by following the DeepMIP protocol; that is, the ocean was initialized from zonally symmetric ocean temperature and a constant salinity of 34.7 psu (Lunt et al., 2017). The simulation was run for 4,000 years until the ocean reached thermodynamic equilibrium, with the final trend of deep-ocean temperature changes lower than 0.05°C per century (Zhang et al., 2020). Monthly averaged velocities (and ocean properties), computed over the last 100 years of the simulation to represent a climatological year, were used to conduct the Lagrangian analyses of the present study. The mesoscale eddy-induced turbulence was parameterized as eddy-induced bolus velocity (Gent & McWilliams, 1990), and these have been explicitly added to the total velocity used in our Lagrangian analysis. This eddy-induced bolus velocity is generally small, with a maximum magnitude of 2 cm/s over regions of low latitude.

The early-Eocene simulation used in this study has been systematically discussed in the context of boundary conditions and detailed ocean circulation, especially in the light of comparison with the present-day situation and also with different CO₂ levels in Zhang et al. (2020). Here we only describe it briefly, regarding (well-concerned) sea surface temperature (SST) and ocean circulation. The simulation reproduces a global mean SST of 28°C, with the annual mean SST varying from 10–15°C in the southernmost Southern Ocean to 30–37°C near the equator (Figure 1). The zonally averaged annual mean SSTs were overall ~10°C warmer than in the present-day simulation (PI-1x, performed with the IPSL-CM5A2, but with the present-day boundary condition), with the largest differences of 12°C found in the Southern Ocean. Wide seasonal variations further extended the highest summer temperature in southern high latitudes to 25°C (Figure 1), reached in the southeast Atlantic-India basin around Australia (Figure 2a of Zhang et al., 2020). This overall warmth and enhanced Southern Ocean temperature bring them generally close to the proxy reconstruction despite some exceptions. The mismatched points mainly include the Tex⁸⁶ biomarker records from the

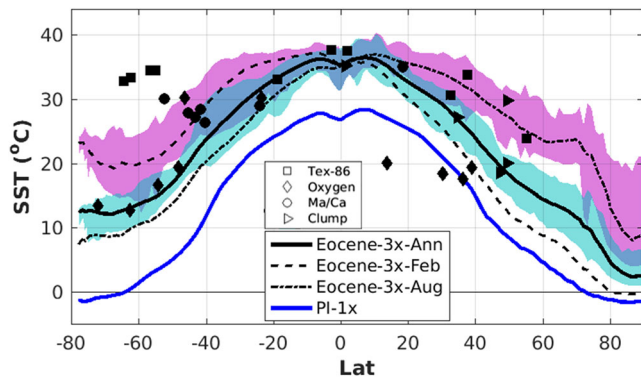


Figure 1. Simulated SST as a function of latitude and comparison with proxy-based temperature reconstructions. Annual mean (solid black), February (dashed), and August (dotted) are shown for the early Eocene; annual mean for the present day is shown as the blue line. The different markers show reconstructed temperatures from different proxies. Shading indicates the simulated SST range over all longitudes.

Southern Ocean at latitude 60°S that suggest the same temperature (30°C) as the equator (Figure 1), which nevertheless has been very likely overestimated (Hollis et al., 2019). Zhang et al. (2020) compared this simulated temperature site-by-site with the Eocene temperature records from the most comprehensive temperature dataset in Hollis et al. (2019). The model-data comparisons suggest that they are generally compatible, although certain differences can be seen for some specific proxy data points. For instance, proxy-based temperature data and simulated temperature show better consistency in the Atlantic-Indian basin than in the Pacific where the model produced more homogenous temperatures, in contrast to large spatial variability suggested by the proxy data (Figures 2a and S2A of Zhang et al., 2020). Zhang et al. (2020) carried out extensive model-data comparisons using statistical methods, such as the root-mean-square deviation (RMSD) and benchmarks following Kennedy-Asser et al. (2020) method. These comparisons suggest that the performance of the model simulation is generally satisfactory, because the data-model RMSD was of the same order of magnitude as the uncertainty of proxy-based SST estimates, and the simulation was able to capture the global mean temperature and some latitudinal gradient patterns from the benchmark analysis.

Models simulations for the Eocene usually could not be able to simulate the much reduced meridional temperature gradient suggested by proxy data (the “equable climate problem”, Huber & Caballero, 2011, and references herein). Regarding this long-standing issue, the early-Eocene IPSL simulation produces a SST gradient from the equator to the Southern Ocean of ~24°C in the annual mean and 18°C in February (Figure 1), leading to an only slightly reduced gradient compared with the present-day 28°C. Comparison with other model results suggests that the meridional temperature gradient in the IPSL-CM5A2 simulation is located in the upper end of the multi-model range (e.g., Hutchinson et al., 2018; Lunt et al., 2012, 2020). Nevertheless, more recent studies appear to suggest a mitigated model-data discrepancy (Cramwinckel et al., 2018; Lunt et al., 2020). Cramwinckel et al. (2018) recently updated the Eocene equatorial SSTs estimation with new proxy, that reduce the temperature gradient to about 20–22°C, and Lunt et al. (2020) found similar values in recent DeepMIP simulations. Reasons for the remaining mismatches, especially on a regional scale, perhaps involve either model simulations, which may still underestimate some regional scale variations, or proxy-based temperature reconstruction, because they can be scrambled by vertically varying processes in the water column (e.g., Ho & Laepple, 2016) and by seasonality signals over high latitudes (e.g., Davies et al., 2019). Overall, despite sizeable uncertainties, the Eocene simulation is nonetheless able to capture the basic temperature pattern suggested by most proxy records and previous model studies.

This paragraph will briefly evaluate the simulated Eocene oceanic circulation in comparison with other models’ results and with proxy-based oceanic circulation reconstruction of the Eocene. The simulation shows a well-ventilated Southern Ocean and a single anticlockwise global overturning cell, with bottom/deepwater formation at high latitudes of the Southern Ocean where dense paleo-AABW sinks into the depths and fills the whole ocean basins (Figure 2a, redrawn from Zhang et al., 2020). This single MOC structure has been well investigated, in relation with winter convection and deepwater formation, in comparison with the PI circulation, and shown to be robust to different atmospheric CO₂ levels (Zhang et al., 2020). Although the magnitude of the MOC can vary in some model results, this well-ventilated Southern Ocean and anticlockwise Southern Ocean MOC pattern are common features of most model results for the early Eocene or middle-to-late Eocene before the Oligocene transition (e.g., Baatsen et al., 2018; Lunt et al., 2010). One exception is a simulation of the GFDL model with 38 Ma bathymetry and boundary conditions, which produces a two-cell MOC with deep water formed in both the Southern Ocean and the North Pacific (Hutchinson et al., 2018). The presence of deepwater formation in the North Pacific in this GFDL simulation (in contrast with the IPSL-CM5A2 simulation used herein and several others) is probably due to its low topography over North America that induces less rainfall over the West Pacific, leading to higher surface density and facilitating deepwater formation (Zhang et al., 2020), as illustrated by sensitivity studies on topography effects (Maffre et al., 2018;

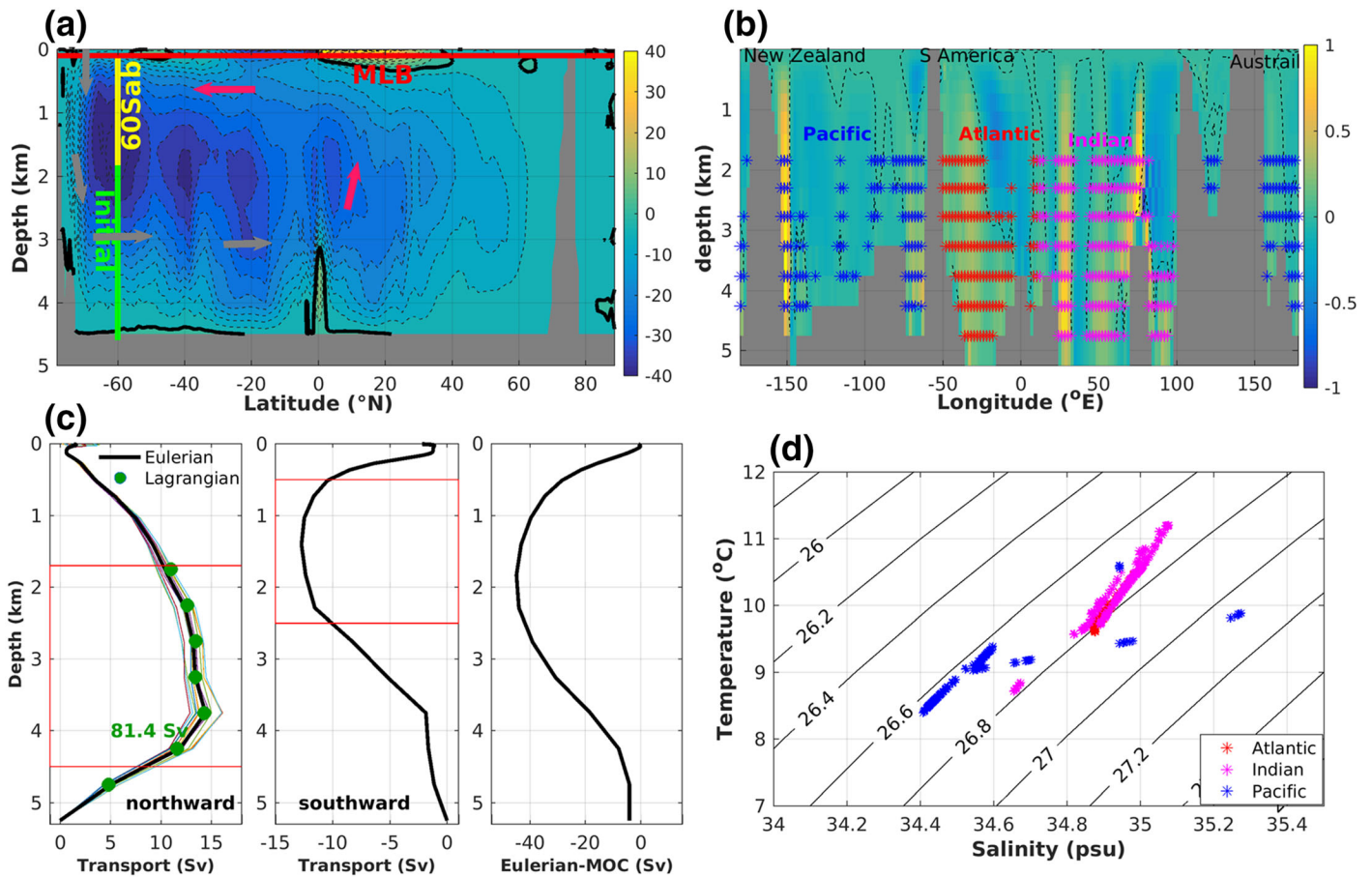


Figure 2. The Lagrangian experiment setup. (a) The specified sections used in the Lagrangian experiment are indicated, including the initial, the 60Ssab (the section above the initial section at latitude 60°S), and the MLB (base of the mixed layer) sections. The Eulerian MOC stream function (Sv) of the early-Eocene simulation (adjusted from Figure 2a of Zhang et al., 2020) is also shown in the background with arrows to schematically indicate the direction of circulation. (b) The initial position of particles is indicated with an asterisk and their relationship to mass transport (with positive values for northward transport and negative values for southward transport in Sv) at the vertical section of 60°S. (c) Particle-based water mass transport estimates (Lagrangian approach) over the lower limb of the MOC, and relationship to Eulerian-inferred transport (integrated along longitude for each layer), including northward and southward transport and the Eulerian MOC stream function at the latitude of 60°S. (d) θ -S diagram of particles (water parcels) at the initial state in the three ocean basins.

Schmittner et al., 2011). Apart from these modeling studies, the MOC has been inferred from neodymium (Nd) isotope distributions, a proxy for ocean circulation (Thomas et al., 2003, 2014). The common features between the simulated and proxy-reconstructed MOC are the well-ventilated Southern Ocean and the predominant Southern Ocean origin of the bottom waters (Thomas et al., 2014). Differences remain in the North Pacific where the ocean is less ventilated in the simulation than as suggested by the proxy data, whereas the Nd-based results suggest that the water of North Pacific origin never crossed the equator. Overall, the well-ventilated Southern Ocean filling the most of the global bottom waters is supported by previous modeling and proxy reconstructions. Further evaluations of the simulation have been addressed in Zhang et al. (2020).

2.2. Lagrangian Experiments and Analysis

2.2.1. Lagrangian Analysis and Ariane Tool

Lagrangian analysis of oceanic model outputs provides an interesting and comprehensive way to investigate the three-dimensional, time-evolving transport fields through a diagnosis of trajectories of virtual particles (Bower et al., 2019; Tamsitt et al., 2018; van Sebille et al., 2018). As a useful and complementary tool to Eulerian approaches, Lagrangian analysis can help answer a range of theoretical and practical questions, as reviewed in Griffa et al. (2007) and more recently in van Sebille et al. (2018). In particular, Lagrangian approach has been widely employed to solve problems involving connectivity between oceanic regions

such as the bottom and the surface layers, and used to track the movement and pathways of various water masses (e.g., Blanke et al., 1999, 2002; Döös et al., 2008; Tamsitt et al., 2017, 2018; van Sebille et al., 2013). Here, we use the Lagrangian analysis to provide comprehensive information on the ocean circulation during the early Eocene, when the bathymetry was tremendously different from the present day. For instance, the much narrower North Atlantic limits deep convection there and the almost closed Drake passage hinders Antarctic Circumpolar Currents (ACC) during the early Eocene, which makes the MOC structure very different from the present day. In addition, divergences of flow within individual basins (Atlantic, Pacific, and Indian oceans) through tropical straits break the mass conservation of each basin and decrease the value of Eulerian-velocity-inferred MOC stream function of individual basins for indicating the overall circulation, which makes the separation of each basin's transport from the total global transport impossible using only a typical Eulerian approach.

Our Lagrangian analysis was carried out using the Ariane tool that is based on an off-line mass-preserving algorithm to compute particles trajectory (<http://www.univ-brest.fr/lpo/ariane>). A detailed description of the method used to follow particles in an Ocean General Circulation Model (OGCM) is given in the appendix of Blanke and Raynaud (1997). The Ariane tool provides a “quantitative” mode that is specifically designed to effectively evaluate water mass transport, by tracking trajectories of particles between an initial section and the other sections which close a three-dimensional oceanic region. Sections can be defined in various ways: geographically (vertical and horizontal cross sections), or in more complex manners, as for example time-dependent isolines of a chosen quantity (isopycnals, mixed layer). Particles are automatically placed by Ariane software tool on each model grid cell of a specified initial section, by considering only water masses flowing inward the closed domain in forward integration (outward the domain in backward integration), and a given water transport is accordingly attached to those particles. Each particle represents a fraction of the total transport through the initial section. Because the transport across the section is not uniform, the water mass transports assigned to particles are different. The algorithm of this transport assignment is that: each grid cell with a given transport T_n is described with N_n particles, and this integer particle number N_n satisfies (Blanke et al., 1999):

$$\frac{T_n}{N_n} \leq T_0 \quad (1)$$

where T_0 is the prescribed maximum transport associated with a single particle. This assignment is made for each time step of the oceanic model data input of Ariane and during a period of time defined for an experiment. The total number of particles is the sum of the N_n over all relevant grid cells of the initial section. Because of the low resolution of the ocean model and the associated rather linear dynamics, we have used a large value for T_0 (0.8 Sv) such that a single particle is released in each grid cell of the initial section at each time step. The setting of this initial section (i.e., velocity fields are sampled only on the initial section) implies that particles should be released everywhere to sample the complete velocity fields of the whole ocean (Blanke et al., 1999; Döös, 1995; Döös et al., 2008).

Subsequently, each particle is tracked over each time step and its trajectory is computed according to the evolving velocity field, until it reaches any one of the specified receptor sections (Blanke & Raynaud, 1997; Döös & Webb, 1994). Along its path, particle velocity, temperature and salinity evolve over the time integration, according to the local Eulerian model fields (Blanke & Raynaud, 1997; Döös & Webb, 1994). Each particle can be seen as a water parcel evolving over time, and the terms particle and water parcel are interchangeably used in this sense. Ultimately, statistical analyses of all these trajectories represent how the water masses are transported from this initial section to another destination. These inter-section transports can be portrayed by means of a Lagrangian stream function (calculation given below), by taking advantage of a mass-preserving scheme (Blanke et al., 1999; Blanke & Raynaud, 1997; Döös, 1995).

2.2.2. Lagrangian Experiment Setup

In the present study, we employ the Ariane tool to trace the fate of the paleo-AABWs and to analyze the dynamical processes contributing to the upwelling along their trajectories. Based on the overall features of the ocean circulation, the initial section (the snapshot) was set in the deep ocean at latitudes 60°S below 1,900 m to sample the northward flowing bottom/deepwater export. The Eulerian-velocity-inferred

meridional stream function (Eulerian MOC) in Figure 2a shows the anticlockwise meridional circulation in the early-Eocene simulation. Surface water loses buoyancy through ocean-atmosphere interaction over the high-latitude Southern Ocean and forms denser water sinking into the depths, then flowing northward in the abyssal ocean and filling the whole ocean basins (Zhang et al., 2020). Therefore, there is a strong net northward export of deep water over the lower (deep) limb of the MOC that is supplied by the deepwater formation in the Southern Ocean and the overall southward transport over the upper ocean. The Eulerian MOC maximum intensity (up to 40 Sv) is reached at 60°S at a depth ~1,900 m, at which latitude and depth the initial section was accordingly set. Zooming into the vertical section at 60°S, the majority of gross northward transport occurs in the abyssal ocean (e.g., northward transport is greater than 10 Sv at depths of 1,800–4,500 m), whereas the southward transport mainly occurs at shallow depths (e.g., 10 Sv for depths of 500–2,500 m) (Figures 2b and 2c). This asynchronous transport over depths closes up the anticlockwise MOC, with a boundary between the upper southward and lower northward transport of ~1,900 m (longitudinally averaged). Correspondingly, the initial section at 60°S was constrained to depths below 1,900 m in the vertical direction. Therefore, this initial section was chosen to sample the northward flowing paleo-AABW mass over the lower limb of the anticlockwise meridional circulation.

To trace the destinations of the paleo-AABW, 4,797 virtual particles were released at the initial section (at 60°S below the depth of 1,900 m), with T_0 value of 0.8 Sv. Particles were released at the middle of each month throughout the first year, according to the monthly evolving velocity fields (only at grid cells where the flow was northward for the given month). The large number of particles leads to a relatively small transport assigned to each particle, ensuring precise representation of the water mass transport. These particles provided a total estimate of 81.0 Sv for the gross northward flowing bottom/deepwater transport over the lower limb of the MOC, which reproduces the Eulerian description of the northward transport very well (Figure 2c). This Lagrangian-based transport estimate was almost twice that of the Eulerian-velocity-inferred MOC value that is the net of two directions flow in the same section. This indicates that half of the northward transports were compensated by their opposing southward transport and the other half left the initial section and carried on toward the north.

These particles 3-D trajectories were integrated for 4,000 years with monthly updated velocity fields until being intercepted by any one of the receptor sections. These receptor sections include the initial section itself, the vertical section above this initial section (60Sab) and the monthly evolving mixed-layer base (MLB), separating the surface homogeneous thermal layer from the deeper stratified ocean below, as shown in Figure 2a. The mixed-layer depth is defined by a potential density difference smaller than 0.3 kg/m^3 with reference to the surface. It has been found that the trajectories at eddies scale and small spatial scales were sensitive to the increasing temporal resolution ranging from days to month, while at scales larger the trajectories were largely independent of the temporal resolution increase from day to month (Iudicone et al., 2002; Qin et al., 2014). Given its $\sim 2^\circ$ spatial resolution, the ocean model used in the IPSL-CM5A2 simulation does not resolve mesoscale eddies (they are parameterized) and the monthly resolution used in the present study is sufficient. Note that the time resolution refers here to the frequency at which the velocity field is updated. Every year, the same climatological monthly velocities are repeated (i.e., after December the velocity fields return to the January), with activated consecutively looped output over time. The Lagrangian experiment was run for 4,000 years to obtain the long-term trajectories of particles. This long-term experiment allowed 99% particles to be intercepted at one of the specific receptor sections. The terms of initial and final refer to the moments when particles are released from the initial section and are received by one of the receptor sections, respectively. Below, we analyze these particles statistically in terms of water mass transport and their corresponding evolution of water properties along their trajectories. In addition to this main experiment, an auxiliary Lagrangian experiment was conducted in a backward mode, in order to trace back the geographical origins, defined as the last point of contact with the surface mixed layer, of these paleo-AABW.

2.2.3. Lagrangian Diagnostics

Two types of diagnostic analysis of the Lagrangian experiment were carried out: Lagrangian stream function and transport-weighted particle distribution.

Lagrangian stream function portrays pathways of water mass on vertical or horizontal directions, by taking advantage of mass conservation (i.e., the corresponding velocity field is non-divergent) (Blanke & Raynaud, 1997; Blanke et al., 1999, 2006; Döös, 1995). The calculation of Lagrangian stream function can be divided

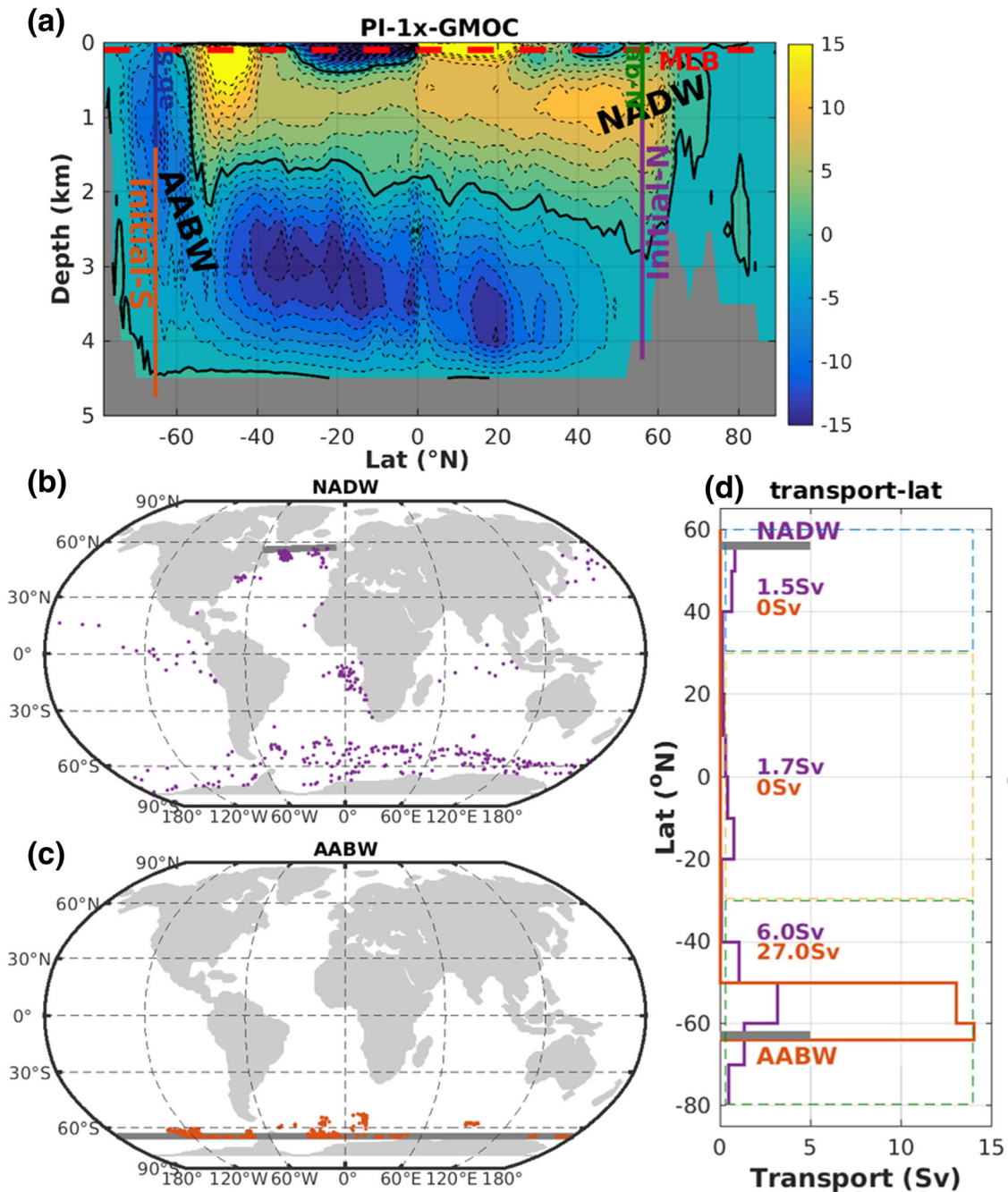


Figure 3. Validation of the Lagrangian method for the present-day (PI) circulation. (a) Setup of two Lagrangian experiments, with background showing the global MOC (CI: 2 Sv) adjusted from Figure 3b of Zhang et al. (2020). (b and c) The final position of particles entering the mixed layer for North Atlantic Deep Water (NADW) and Antarctic Bottom Water (AABW) in turn. (d) Probability distribution as a function of latitude, shown as Sv per 10° latitude band. Initial sections are marked by thick gray lines in (b), (c), and (d).

into three steps (Blanke et al., 1999, 2006; Döös et al., 2008): (1) Obtain a three-dimensional transport field that corresponds to the flow of the water mass within the domain of integration of the trajectories. As the local three-dimensional non-divergence of the flow is exactly preserved, each particle entering one model grid cell through one of its six faces has to leave it, and the transport field satisfies

$$\partial_i T_x + \partial_j T_y + \partial_k T_z = 0 \quad (2)$$

where T_x , T_y , and T_z depict the transports in the three directions, and where i , j , and k refer to the grid index. (2) Obtain trajectories of individual particles by computing the three-dimensional streamlines of the velocity, and achieve the transport fields on the model metrics by algebraically summing the individual particles on each junction of two cells (i.e., recording particles when trajectory crosses grid cell boundaries every time). (3) Compute the stream functions by integrating these transport fields along the vertical or zonal direction, which is similar to the Eulerian stream function calculation. Accordingly, the meridional $\Psi_{j,k}^{LZ}$ and horizontal $\Psi_{i,j}^{LH}$ stream functions are defined as

$$\Psi_{j,k}^{LZ} - \Psi_{j,k-1}^{LZ} = - \sum_i \sum_n T_{i,j,k,n}^y \quad (3)$$

$$\Psi_{i,j}^{LH} - \Psi_{i-1,j}^{LH} = \sum_k \sum_n T_{i,j,k,n}^x \quad (4)$$

Contours of $\Psi_{j,k}^{LZ}$ and $\Psi_{i,j}^{LH}$ depict pathways of water mass movement projected onto the meridional (latitude-depth) and horizontal (longitude-latitude) directions, respectively. Northward and eastward movements are counted positive, while southward and westward movements are counted negative. One advantage of using the Lagrangian stream function is that it can then be decomposed into partial stream functions, computed from trajectories of particles received by a relevant section (Blanke et al., 1999; Döös et al., 2008). The partial Lagrangian stream function is obtained by summing only the particle trajectories intersecting by a selected final section.

To obtain statistical patterns from an ensemble of particles, we use the transport-weighted particle distribution for any variable tagged along the particle trajectories, such as density, potential temperature and salinity. This transport distribution is roughly equivalent to the probability density function (as defined in Equation 1 of Tamsitt et al., 2018), but is weighted by the volume transport of each particle and without any standardization. It is numerically calculated by binning particles and summing their transport in each bin of a given space. The transport distribution in χ space is calculated as

$$P(\chi) = \sum_{i=1}^N \xi_i T_i; \quad \xi_i = \begin{cases} 1, & \text{if } \chi - \frac{\delta}{2} < \chi_i \leq \chi + \frac{\delta}{2} \\ 0, & \text{otherwise} \end{cases} \quad (5)$$

where δ is the bin width, N is the total number of particles, and χ_i is the property of the i^{th} particle. In the following analysis, we replace χ with density, potential temperature, salinity, and depth to analyze particles distribution at the different moments, such as when they are released from and intercepted by a section. For instance, transport distributions of different fates when they are released reveal their tendency to different fates, and the transport distribution differences between the initial and final sections depict transformation/conversion of relevant quantities that particles have gone through along their trajectories.

2.3. Testing the Lagrangian Analysis on the More Constrained Present-Day Conditions

We applied the same Lagrangian analysis framework to present-day conditions (a more constrained framework, and much better known circulation) and compared the results with our current understanding to validate our analysis. For present-day conditions, the meridional circulation is characterized by a two-cell structure with deep water formed both in the North Atlantic and Southern oceans (e.g., Lumpkin & Speer, 2007). Accordingly, we carried out two Lagrangian experiments by releasing particles from two initial sections, that is, initial-N (at 56°N below 750 m) and initial-S (at 65°S below 1,400 m), at the lower limb of the MOC to trace the fates of the NADW and Antarctic Bottom Water (AABW), respectively (Figure 3a). Particles were released from the initial sections equatorward and tracked until they were intercepted by one of the receptor sections that include the initial sections, the sections above (above-S and above-N) and the MLB, following the same approach as for the early Eocene (as described above).

Our investigation examines the NADW and AABW in turn. For each, we first introduce the Lagrangian experiments and then present their results for each deepwater mass, before comparing with our understanding of present-day conditions. For the NADW, 2931 particles sample a total southward transport of 17.0 Sv of

deep water at the initial North Atlantic section at 56°N, of which 7.7 Sv went back to the North Atlantic region, either through the initial section itself or the section above (i.e., the above-N section in Figure 3a). The remaining 9.2 Sv of water (more than half) leaves the North Atlantic and eventually crosses the MLB entering the surface thermal layer globally. The final locations where these NADW enter the mixed layer are shown in Figure 3b: A large part of NADW enters the thermocline in the Southern Ocean scattered over the Atlantic, Indian and Pacific sectors. The transport distribution of NADW as a function of latitude (Figure 3d, calculated from Equation 5) shows that the majority (6 Sv out of 9.2 Sv) came to the surface over the southern high latitudes, through the well-known wind-driven upwelling in the Southern Ocean. Around 3 Sv of particles reached the surface ocean over other regions, including tropical upwelling (mainly along eastern boundaries) and the ventilation in the North Atlantic and few in the North Pacific. These Lagrangian experiment results on the fates of the NADW highlighted the role of the upwelling branch of the MOC in the Southern Ocean, and fit our understanding of global circulations well.

Numerous studies, from multiple perspectives, have highlighted the role of Southern Ocean upwelling, which is driven by strong westerlies across all longitudes, in closing the present-day MOC (Blanke et al., 2002; Garzoli & Matano, 2011; Marshall & Speer, 2012; Rhein et al., 2015; Wolfe & Cessi, 2014). For instance, the inter-hemisphere pole-to-pole meridional circulation has been illustrated from a physical dynamics perspective (e.g., Toggweiler & Samuels, 1998; Wolfe & Cessi, 2011). Marshall and Speer (2012) further demonstrated that the Atlantic deep water is brought to the surface via the Southern Ocean upwelling through inter-hemisphere overturning circulation, based on observation data and numerical experiments. Using the Lagrangian analysis, Blanke et al. (2002) showed that the Southern Ocean is an important receptacle of deep water. More recently, Tamsitt et al. (2017) demonstrated that the northern-sourced deep water (i.e., NADW) of the three ocean basins spiraling southeastward and upward through the ACC, with enhanced upwelling at major topographic features. Rhein et al. (2015) used chlorofluorocarbon (CFC) observations in the Atlantic to examine the spreading velocity and pathways of Labrador Seawater and overflow water from Denmark Strait, and found that Deep Western Boundary Current is the fast pathway reaching the Southern Ocean.

For AABW, the total amount of 34.5 Sv northward flowing water was captured in the lower limb of the MOC, which is much larger than the net northward transport of ~10 Sv shown by the Eulerian MOC stream function. This large amount of northward transport can be attributed to deep water formed locally that leads to compensation in the wide Southern Ocean basin (as in MOC stream function). Of that amount of northward deep water, 7.5 Sv returned to the initial section, and the majority, up to 27 Sv, crossed the MLB and came out into the surface ocean. The final locations where these particles cross the MLB are restricted to the Southern Ocean with the most northern position of 40°S. This may be in line with an explanation that AABW is isolated from surface ocean by the overlying NADW and it mixes with the southward NADW in the interior (Marshall & Speer, 2012; Orsi et al., 1999). The southern component of this mixed upwelled water mass goes almost immediately back into the deep ocean, forming the recirculation of water between the Antarctic water masses and Circumpolar Deep Water (Gordon, 1971; Johnson, 2008; Orsi et al., 1999; Tamsitt et al., 2017; Toggweiler et al., 2006). Therefore, the results of our Lagrangian analysis for the fate of NADW and AABW are in good agreement with the actual understanding of the global circulation under present-day conditions, confirming the interest to apply such Lagrangian analysis to the Eocene circulation.

3. Results

3.1. Diagnostic Analysis of the Paleo-AABW Source and of the Initial State

A diagnostic analysis of the source supplying the paleo-AABW mass at the lower limb of the MOC can illustrate how the northward export of paleo-AABW is sustained, bringing valuable insight into paleo-AABW dynamics. Further, probability distribution analysis of the initial state of the water mass properties, such as temperature, salinity and density (at the initial section), can assess the representativeness of virtual particles and record the starting point of these properties.

These paleo-AABW exports are largely supplied by the ocean subduction process associated with winter ventilation over the high-latitude Southern Ocean. The auxiliary backward experiment provided an estimate of 81.0 Sv for the total gross amount of water crossing the initial section, of which 49.8 Sv originated from the surface ocean by crossing the MLB over the Southern Ocean (Table 1). This total gross transport is exactly

Table 1
Origins and Fates (in Sv) of Northward Flowing Antarctic Bottom Water (paleo-AABW), and Their Distribution Across the Three Basins

	Origins			Fates						
	Initial	60Sab	MLB_SO	Initial gross	Initial	60Sab	MLB			
							Global	Pacific	Atlantic	Indian
Global	28.17	3.04	49.84	81.04	34.90	25.35	20.73 (100%)	9.72 (44.4%)	8.49 (41.1%)	3.07 (15.0%)
Pacific	—	—	9.69	24.45	11.06	9.04	4.35 (100%)	2.47 (58.1%)	1.44 (32.6%)	0.44 (9.3%)
Atlantic	—	—	16.14	18.75	3.10	20.74	7.57 (100%)	2.98 (34.1%)	4.77 (54.5%)	1.05 (12.5%)
Indian	—	—	24.01	37.84	20.74	9.50	4.35 (100%)	3.72 (48.7%)	2.28 (30.3%)	1.58 (21.1%)

Note. Initial: 60°S section below 1,900 m; 60Sab, 60°S section above 1,900 m; MLB, the base of the mixed layer. The left part (Origins columns) refers to the auxiliary backward Lagrangian experiment. The right part (Fates columns) refers to the forward Lagrangian experiment. The middle column (Initial gross) refers to both. The transport of paleo-AABW upwelling in the mixed layer (MLB columns) is further decomposed among the three basins (last three columns). These diagnostics illustrate the inter-basin exchanges, with the gray shading highlighting the proportion that stays within the same basin.

the same as the water transport from the initial section in the main Lagrangian experiment (i.e., tracing the fates of paleo-AABW). The statistical analysis on geographical locations of the last contact point reveals that the Atlantic-Indian sector of the Southern Ocean are the main sources of paleo-AABW (Table 1), providing more than 80%. The rest of the paleo-AABW parcels stem from the Pacific basin. This origin-tracking analysis also suggests that the majority of deepwater formation is supplied by local processes, with deep convection, deepwater formation and northward export occurring in the same basin. The only exception is the Atlantic sector of the Southern Ocean, because the denser water of Atlantic origin is partly exported eastward to the Indian Ocean sector due to the lack of bathymetry barriers. Regarding the timescale, the occurrence of this ventilation is relatively fast, since 80% of AABW originating from the mixed layer have completed their journey to 50°S within 20 years.

The Lagrangian experiment estimates paleo-AABW transport very well compared with the Eulerian description (Figure 2c), confirming the adequate particle sampling strategy. A large part of this northward flowing deep water starts its journey in the Atlantic-Indian sector of the Southern Ocean (Table 1 and Figure 2b). Within each basin, there is a clear west-east pattern with the majority of deepwater parcels leaving the initial section from the west side of the basin (Figure 2b), within western boundary currents. This west-east pattern across the basin is consistent with the clockwise subpolar gyre circulation in the horizontal plane, as shown by the Eulerian barotropic stream function (Zhang et al., 2020).

There are no distinct differences in potential density (σ_0) of the northward flowing water masses among the three basins. The potential temperature-salinity (θ -S) diagram of water mass shows that the potential density anomalies of the paleo-AABW are in the range of 26.6–27 kg/m³ when leaving the initial section (Figure 2d); these values are comparable to the typical value of the interior ocean of 26.5 kg/m³ (bulk volume of seawater) of the early-Eocene simulation. The density differences among the three basins are relatively small (i.e., within 0.5 kg/m³), due to the compensating effect of changes in temperature and salinity. For instance, the Pacific paleo-AABW with lower temperature (by 1.5°C) and lower salinity (by 0.2–0.3 psu) is less than 0.2 kg/m³ lighter than the paleo-AABW from the Atlantic sector. The Indian sector paleo-AABW shows no density differences from the deepwater mass of the Atlantic basin, with an average of ~26.7 kg/m³.

3.2. Fates of Paleo-AABW and Their Pathway

3.2.1. Two Fates of Paleo-AABW

Northward flowing deepwater mass over the lower limb of the MOC shows two fates: (1) entering into the surface ocean by crossing the MLB and (2) returning to the Southern Ocean across 60°S, either through the initial section (below 1,900 m depth) or the section above (the 60Sab section). One way to quantitatively elucidate the fate of paleo-AABW mass is to statistically analyze the initial and final position of these water parcels. As shown in Table 1, the statistical results indicate that more than a quarter of paleo-AABW parcels enter the surface ocean by crossing the MLB, with an average travel time around 700 years (Figure S2); nearly half return to the initial section within 100 years; and the rest are intercepted by the 60Sab section with a travel time of 300 years.

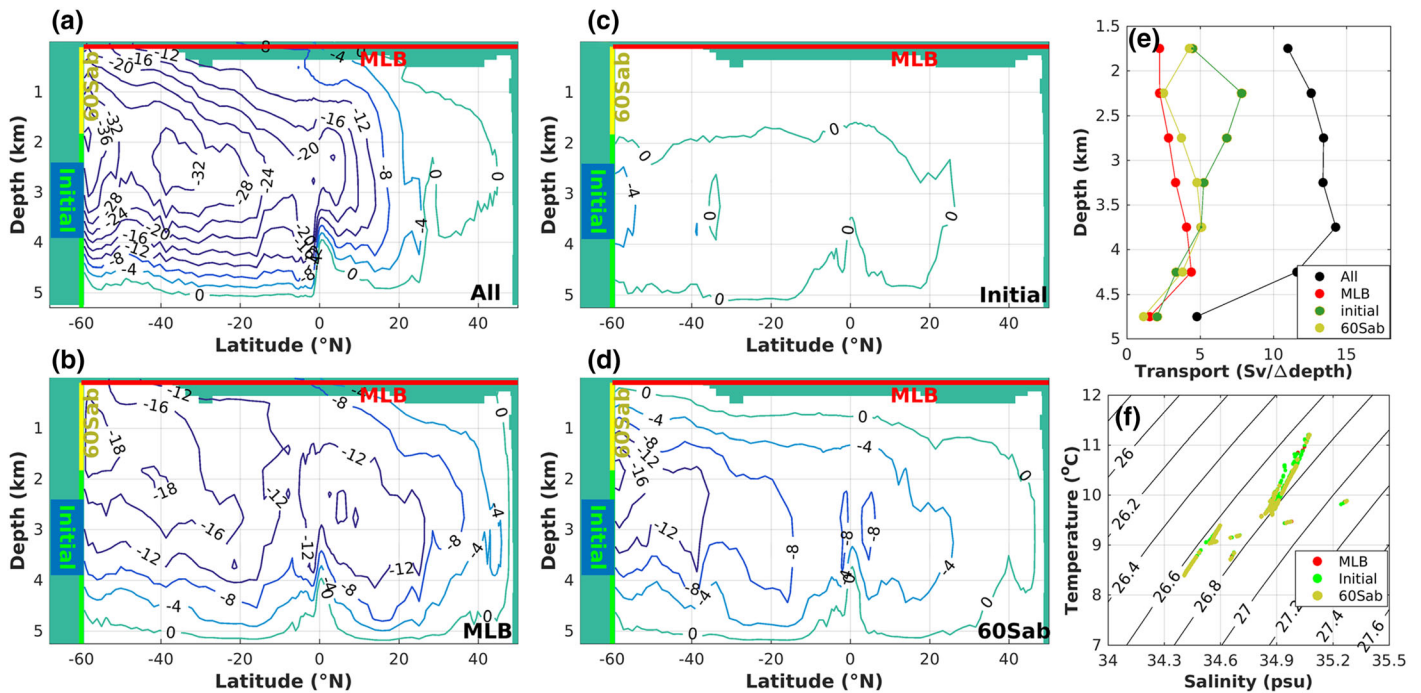


Figure 4. Fates of northward flowing paleo-Antarctic Bottom Water. Meridional Lagrangian stream functions show the zonally integrated transport of paleo-AABW, (a) for all particles, (b) for particles crossing the MLB; for particles back to the Southern Ocean through (c) the initial deep section and (d) through the upper 60°Sal section (60Sab), respectively. (e) Transport distribution of paleo-AABW toward the different final sections as a function of their initial depth at 60°S. (f) θ -S diagram of water particles at the initial 60°S section, colored according to their fates.

Another way to illustrate the fates of this paleo-AABW mass is to calculate the meridional Lagrangian stream function from these water parcels all along their trajectory, which gives more information on their temporal evolution along their trajectories in addition to the initial and final stage. It is worth to notice that this meridional Lagrangian stream function represents only a fraction (i.e., the water flow originating from paleo-AABW) of the Eulerian-velocity-inferred MOC stream function, because water particles are released only from the lower limb of the MOC in our Lagrangian experiment. Theoretically, taking a full range of particles released from all grid cells in the full-domain simulation into consideration will reproduce a Lagrangian stream function that is exactly the same as the Eulerian MOC stream function (Blanke & Raynaud, 1997; Blanke et al., 1999; Speich et al., 2001). The Lagrangian MOC stream function for all particles (Figure 4a, calculated from Equation 3) suggests that around 40 Sv of water, indicated by the difference between the bottom and the top of the section, was transported away from the initial section toward the north. Along its journey northward, more and more water is transported upward, and either enters the surface ocean after crossing the MLB or changes direction to the south to eventually reach the 60Sab section. Similarly, the total stream function (Figure 4) shows that more than 15 Sv of paleo-AABW enters the surface ocean and ~25 Sv of water goes back to the Southern Ocean through the 60Sab section. Along the latitudinal direction, there is about 20 Sv of paleo-AABW that crosses the equator, and around 15 Sv continues on to latitude 20°N. This meridional Lagrangian stream function can be decomposed into partial stream functions for the particles that go back to the Southern Ocean, and those intercepting the MLB separately (Figures 4b–4d).

Under PI conditions, the proportion of deepwater mass entering the surface mixed layer (Table S2) is larger than that (25%) for the early-Eocene simulation, with 9 Sv out of the 17 Sv for NADW and 27 Sv out of the 35 Sv for AABW. These large proportions are probably due to the presence of the Antarctic Circumpolar Current, dragging the NADW through inter-hemisphere circulations (e.g., Wolfe & Cessi, 2011) and may also induce meridional excursion for AABW, because circumpolar circulation in the Southern Ocean is not strictly zonal (Tamsitt et al., 2017; Volkov et al., 2010).

3.2.2. What Drives the Different Fates of Paleo-AABW?

Particles sampling the paleo-AABW show different fates depending on their initial depth and their basin of origin. Figure 4e shows the transport distribution of particles as a function of initial depth. The results suggest that water parcels originating in the deepest layers (4,000–4,500 m) are relatively more likely to be intercepted by the MLB, the lower part of the deep waters (3,500–4,000 m) tend to be intercepted by the 60Sab section, whereas the upper part of the deep waters (2,000–3,000 m) tend to return to the initial section. This depth dependency was unexpected, because, intuitively, the upper deep waters have a short distance to travel before reaching the MLB, thus should have a higher chance of being intercepted by the MLB. There are two possible explanations for this unexpected result: (1) The switch between northward flowing and southward flowing transport happens somewhere in the middle of the lower and upper deep water, making it more likely for the paleo-AABW flowing in the lower part of the deep waters to return to the initial section, and (2) a “channel” (e.g., prevailing upwelling) may link the upper deep waters to the surface ocean.

Among the different basins, the waters of Atlantic origin are more likely to enter the mixed layer (7.6 out of 18.8 Sv) than that of the Indian (4.4 out of 20.7 Sv) and Pacific (4.4 out of 11.1 Sv) oceans (Table 1). Most paleo-AABW of Pacific and Indian Ocean origin return to the initial section: 45% and 55%, respectively (Table 1). In contrast to this spatial pattern, there are no distinct patterns among these destinations in terms of initial salinity or temperature, as shown in the θ -S diagram (Figure 4f).

3.3. Return of Paleo-AABW to the Surface Ocean by Crossing the MLB

As mentioned above, a quarter of paleo-AABW parcels cross the mixed layer and eventually return to the surface ocean, which is statistically represented by particles intercepting the MLB (Figure 4b). The trajectories of these deepwater parcels ending in the mixed layer illustrate the pathways toward the surface ocean and the actual transformations of paleo-AABW into light water. The amount of this deepwater crossing the MLB is up to half of the non-recirculating paleo-AABW mass (20.7 Sv out of 46.1 Sv). This large proportion shows this upwelling toward the mixed layer plays a crucial role in closing up the MOC. We will investigate further in more details what are the main dynamical processes occurring along the particle trajectory for this obduction of deep water.

3.3.1. General Routes and Residence Time of Deep Water Toward the MLB

From the initial section onward, general routes for the horizontal propagation of these paleo-AABW ending in the mixed layer are shown by the barotropic Lagrangian stream function (calculated from Equation 4, Figure 5a). The results show varied water transport routes among different basins. Over the Pacific sector, ~5 Sv of paleo-AABW leaves the Southern Ocean from the initial section and eventually crosses the MLB and returns to the surface ocean. A small fraction of these northward flowing water masses branches off from the northward transport and joins the southwest currents into the Indian basin before reaching the equator. Around half of these northward flowing water masses come out into the surface mixed layer over the tropics (9.3 Sv). The remaining small fraction continues its northward journey crossing the equator and eventually reaching the surface ocean over the northern high-latitude regions with deeper mixed-layer base (Figure 4 of Zhang et al., 2020). In the Atlantic-Indian Ocean, paleo-AABW particles initially travel toward the north, and most reach the tropical region. Over the equatorial region of the Indian Ocean, a large fraction of water parcels changes their direction toward the west and crosses the remaining Tethys Sea (bounded by Africa-India in the south and Eurasia in the north). There are actually two fates for these waters flowing westward: (1) Around 5 Sv goes southward along the east coast of the paleo-Indian continent, and (2) 10 Sv water keeps traveling westward, crossing the Gibraltar Strait and being transported southward afterward, forming the noticeable anticlockwise transport around the African continent. In the Atlantic, the water parcels continue their journey northward reaching the equatorial region, travel anticyclonically in the subtropical regions and return to the south through the flow along the west coast of Africa.

Strong tropical upwelling over the Pacific basin is supplied by deep water originating from multiple basins, including paleo-AABW of Pacific origin locally, paleo-AABW of Atlantic origin transported from the east through the Panama Strait and paleo-AABW of Indian origin from the southwest. About 5 Sv water transport toward the Atlantic basin crossing the Panama Strait is also visible in these routes of deepwater crossing the MLB, as indicated by the differences in the Lagrangian stream function (Figure 5). Although this only

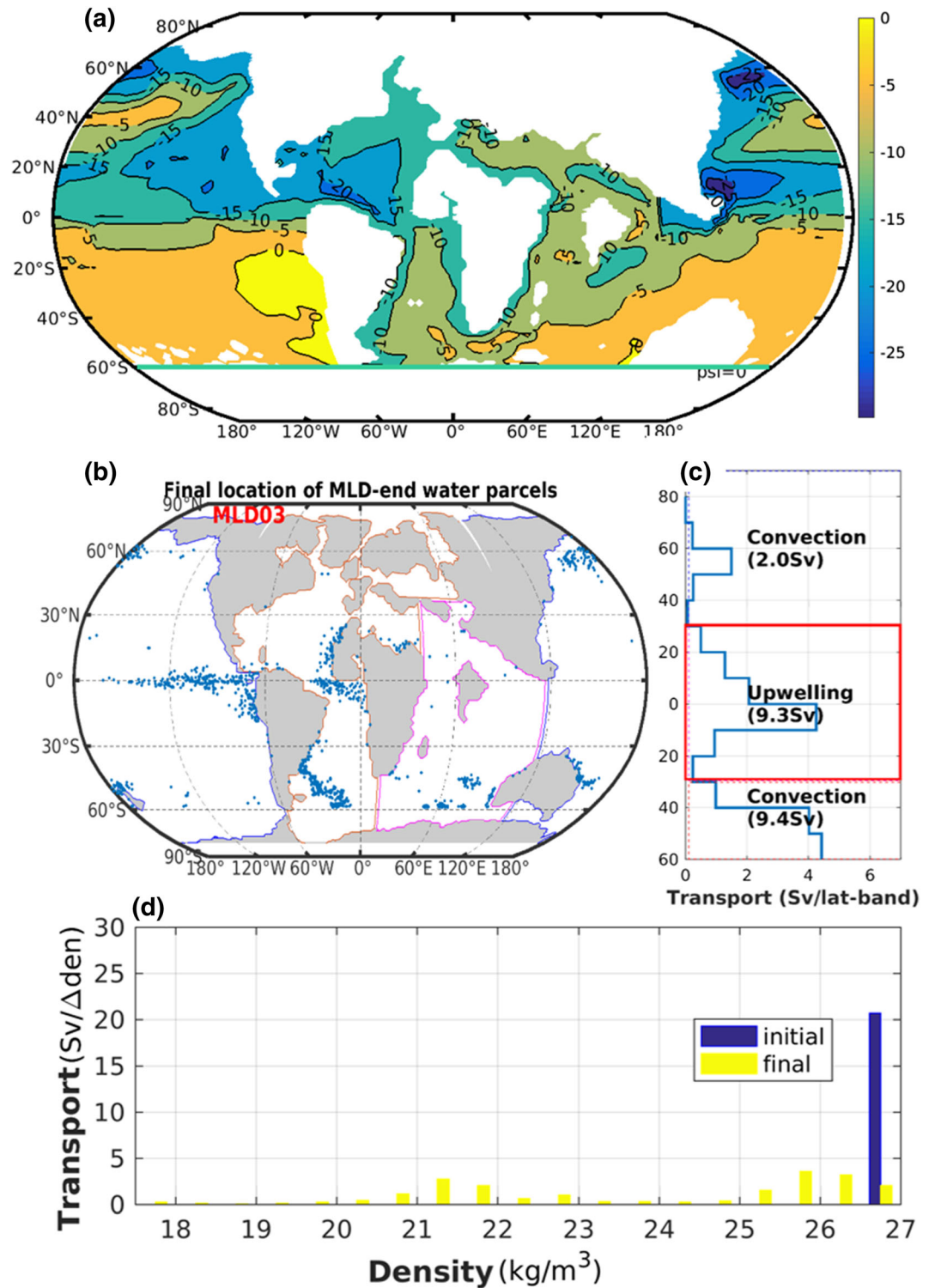


Figure 5. Horizontal pathway of paleo-AABW for particles entering the mixed layer. (a) Horizontal Lagrangian stream function (in Sv), illustrating their pathways toward the mixed layer. (b) Final location of the paleo-AABW particles entering the mixed layer, with basin contours in color. (c) Upward transport distribution of paleo-AABW particles across the mixed layer, in Sv per 10° latitude band. (d) Transport distribution (Sv per density bin, particle number weighted by volume transport) of water parcels as a function of initial (blue) and final (yellow) potential density anomaly in 0.5 kg/m³ bins.

partially represents the net water transport across the strait, the direction seems compatible with studies on a more recent opening of the strait (Nof & Gorder, 2003; Sepulchre et al., 2014; Tan et al., 2017).

The final geographical location of where paleo-AABW parcels cross the MLB shows a clear latitudinal pattern (Figure 5b). The distribution of these water parcels in terms of volume flux as a function of latitude highlights over three regions: Southern Ocean deep convection, equatorial/tropical upwelling, and Northern Hemisphere high latitudes (NHH) (Figure 5c). The Southern Ocean convection is revealed by enhanced vertical diffusivity and deep mixed-layer depth. For the equatorial/tropical upwelling regions, water parcels enter the surface mixed layer mainly along the equator (Pacific and Atlantic), and over the eastern coastal regions in the Pacific and Atlantic basins, where surface winds drive strong offshore Ekman transport. The averaged time required to travel from the initial section to the MLB accordingly decreases from the north toward the south, with 1,400 years for the NHH region, 1,200 years for the tropics, and 900 years for the Southern Ocean. On average, 80% of the deepwater parcels crossing the MLB finish their journey within 1,000 years (Figure S1).

3.3.2. The Role of Tropical Upwelling in Deepwater Obduction

The important role of tropical upwelling in the deepwater obduction in the early-Eocene simulation is highlighted by the large amount of upwelling water in the tropical regions. As shown in Figures 5b and 5c, the amount of paleo-AABW upwelling in the tropical region is up to 9.3 Sv, which consists of 45% of the total deepwater masses crossing the MLB. This upwelling is associated with the upwelling branch of the Eulerian MOC stream function in this tropical region (see Figure 7c, between 300 and 1,000 m). This large fraction indicates that the contribution of tropical upwelling to the deepwater obduction process is substantial in magnitude, which is essential for closing the global ocean circulation. The rest of the particles mainly reaches the mixed layer through vigorous ventilation in the Southern Ocean.

The strong upwelling over tropical regions is generally consistent with the spatial pattern of wind-driven Ekman pumping. With the easterlies blowing over the tropical surface, westward flowing water is dragged by the Coriolis force away from its original westward route on both sides of the equator. The opposite directions of the Coriolis force between the southern and Northern Hemisphere result in divergences of surface water transport over the equatorial region and induce the well-known Ekman pumping. In line with this, the Ekman pumping can explain the spatial pattern of the particles final positions when entering the surface mixed layer. As shown in Figure 5b, water parcels enter the surface mixed layer mainly over the eastern coastal regions, where surface waters are dragged offshore by wind, leading to divergence at the surface and inducing coastal upwelling.

To further put this tropical upwelling in context, we compared it with PI conditions. First, we need determine which deepwater mass (NADW or AABW) is more comparable to the paleo-AABW in the early-Eocene simulation. Intuitively, the AABW is the natural counterpart for the early-Eocene paleo-AABW, because both share the same origin in the Southern Ocean. However, the overlying NADW in the present conditions complicates and even hinders these direct comparisons. In contrast, from the actual ocean circulation perspective, the NADW is a more comparable alternative, because it is formed in high latitudes (albeit in opposite hemispheres) and has direct access to the surface ocean. However, only 1.7 Sv (out of 9.2 Sv) of the southward flowing NADW comes out into the surface ocean in tropical regions and the majority returns to the surface ocean through the Southern Ocean upwelling. Therefore, compared with PI conditions, the proportion (9 Sv out of 21 Sv) of tropical upwelling of paleo-AABW into the surface ocean during the early Eocene is much larger. This is in line with the stronger Eocene upwelling over the tropics than the present day (Figure S6b). Indeed, because of the almost closed Drake passage, there is no Antarctic Circumpolar Current in the Eocene, and the tropical gateways between the different basins are not located in the westerlies latitude band, such that the paleo-AABW overturning cell cannot function as a pole-to-pole circulation like the NADW today. Consequently, another transformation route to surface waters needs to be found, and this is partly through equatorial and tropical upwelling.

3.3.3. Intense Exchanges Across the Three Basins

The strong connection between the three basins can be seen from the well-mixed final locations of particles, independently of their basin of origin at the initial section. As summarized statistically in the right part of Table 1, only half the amount of deepwater parcels enter the mixed layer in the same basin as they departed from, while the other half enters the surface ocean in other basins. This initial-final analysis provides only a

minimum estimate on exchanges between basins, because some of water parcels that eventually end up in the same basin may travel to other basins before reaching their final location. In addition, the amount of paleo-AABW water ending in the Pacific mixed layer is more than twice as the amount of paleo-AABW initialized from this basin (9.7 vs. 4.4 Sv), demonstrating that deep waters ending in the Pacific mixed layer are supplied from multiple basins, that is, the Pacific itself, the Atlantic, and the Indian Ocean. Overall, these Lagrangian-based statistics illustrate that the magnitude of inter-basin overturning transports is substantial.

4. Discussion

4.1. Conversion of Paleo-AABW Into Lighter Surface Water

The principle of deepwater conversion is that deep water is transferred from the interior ocean to the surface mixed layer by both diapycnal mixing (Munk, 1966) and obduction processes (Blanke et al., 2002; Liu & Huang, 2012; Marshall & Speer, 2012). The mass flux escaping the interior ocean in our Lagrangian experiment is documented by particles intercepted by the MLB. During their journey, the physical characteristics of water parcels are modified by mixing with surrounding water, in association with topographical interactions and mesoscale dynamics (Rimaud et al., 2012). Tracing the evolution of properties of these water masses along the trajectory can thus illustrate how these processes contribute to paleo-AABW conversion.

4.1.1. Deepwater Conversion Accompanied by Density Transformation

For those water parcels that eventually enter the surface ocean, most go through diapycnal mixing processes with net negative density transformation during the journey, as shown by the differences of their transport distribution of density anomaly between the initial and final state (Figure 5d). At the initial section, paleo-AABW density falls in the range of 26.5–27 kg/m³, whereas their density anomaly when they enter the mixed layer ranges from 17 to 27 kg/m³ with one mode at 21–22 kg/m³ and another around 26 kg/m³. Therefore, water mass density decreases conspicuously from the initial to the final state, indicating that water parcels go through negative density transformation along their journey. Actually, the net negative density transformation are the results of two opposing processes: salinity and heat changes, as a result of mixing with the surrounding waters. The majority of water parcels gain both salinity and heat at the same time along their journey, but the latter dominates the density decrease, as shown by the probability distribution in the salinity and temperature spaces (Figure S3).

The following analysis on the full-range trajectory of water parcels allows us to pin down where these processes happen exactly. Density changes along the water parcels' trajectory reveal clear vertical and geographical patterns. In the vertical direction, the density transformation mostly occurs in the upper ocean, whereas in the abyssal ocean, water parcels mostly travel along isopycnals with conserved density. The scatterplot of density changes as a function of depth (Figure 6a) shows considerable changes over the upper ocean (e.g., above 1,000 m), but very weak changes below the depth of 1,500 m. For the upper ocean, the particles distribution as a function of density change (Figure 6b) is clearly skewed to the left, indicating overall net density loss. The net negative density transformation is the balance of the density loss and density gain, with the latter being much smaller in extent. Further investigation reveals that these positive values of density change are due to the seasonal cycle effects, and examining the density changes at annual frequency filters this out and shows negative density change along the trajectories (Figure S4). Comparisons of density changes among different vertical layers demonstrate a clear decrease in this net density transformation with increasing depths. For instance, over the top 500 m there are four times as many particles losing density larger than 0.025 kg/m³ per month than over the 500–1,000 m depth range (Figure 6b).

In line with this efficient density transformation in the upper ocean, the final depths where water parcels reach the MLB are restricted to the upper 500 m. In contrast, the final depths of the particles that do not experience significant density changes (defined as the final density ≥ 26.5 kg/m³) vary from 100 to 2,800 m, and are geographically limited to within 50°S south. The geographical distributions of these two types of water parcels are consistent with the findings of Blanke et al. (2002), who found that deepwater masses enter the surface ocean in two ways: (1) Deepwater parcels accumulate upward displacement over time and eventually reach the surface mixed ocean throughout the climatological year, and (2) seasonal shallowing of the mixed layer can absorb some water into the surface mixed ocean, leading to water transfer into the mixed layer. In the horizontal direction, the large density change mainly occurs near the tropical upwelling regions (Figure 6c), primarily in response to wind-driven Ekman transport. Figure 6c presents the

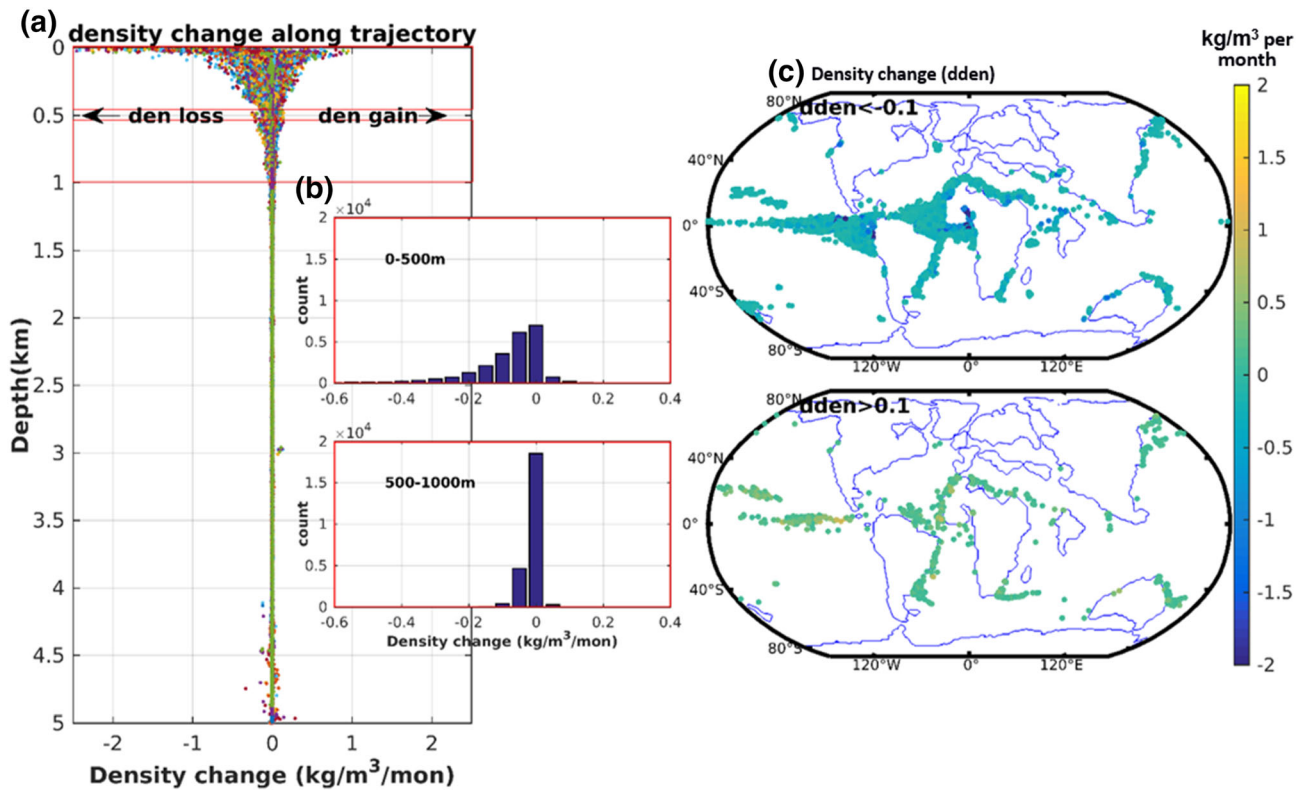


Figure 6. Density transformation along full-range trajectory of paleo-AABW parcels entering the mixed layer. (a) Scatterplot of density change (kg/m^3 per month) as a function of depth. (b) Probability distribution as a function of density change at the two vertical layers as indicated in Figure 6a, with the per density change bin of 0.05 kg/m^3 . (c) Geographical location of large density transformations, shown as the geographical scatterplots of water parcels whose density change is greater than 0.1 kg/m^3 or less than -0.1 kg/m^3 .

geographical distribution of these water parcels whose density change is greater than 0.1 kg/m^3 per month. Although both density gain and loss related to seasonal cycle are found near the tropics (Figure 6c), the annual signal is dominated by a net density loss (Figure S6b). This strong negative density loss over the tropical regions matches the tropical upwelling pattern well, supporting its role in density transformation. Some density transformations also occur over the high-latitude regions, probably as results of strong air-sea flux and induced convective displacement/ventilation of water parcels, but their contribution remains relatively small.

This efficient density transformation in the upper ocean is coupled to the effective net upward transport at the similar vertical level. As illustrated by the depth changes as a function of depth along the particle trajectories (Figure 7a), the net upwelling mainly occurs in the upper ocean, despite an overall small absolute change. In the upper ocean, the particles distribution as a function of depth change (Figure 7b) is strongly left-skewed, indicating substantial net upwelling. In contrast, despite the larger absolute vertical displacements (both upward and downward transport) in the abyssal ocean, these two opposite displacements are of similar order of magnitude and therefore cancel each other out, without causing net upwelling transport. These large absolute vertical displacements in the abyssal ocean are probably due to seafloor perturbations, since the spatial pattern matches the bathymetry very well (Figure S5).

4.1.2. The Tropical Upwelling of Paleo-AABW

The above analysis of particle trajectory demonstrates that important processes occur over the tropical region, highlighting the importance of tropical upwelling in the obduction of paleo-AABW. This section will focus on this tropical upwelling transport to investigate the mechanism behind this prevailing upwelling and the potential analog to the present-day situation.

Apart from statistical summaries of the final transport over tropical regions, another way to show vertical transport is to calculate actual vertical transport at each depth using the MOC stream function. By

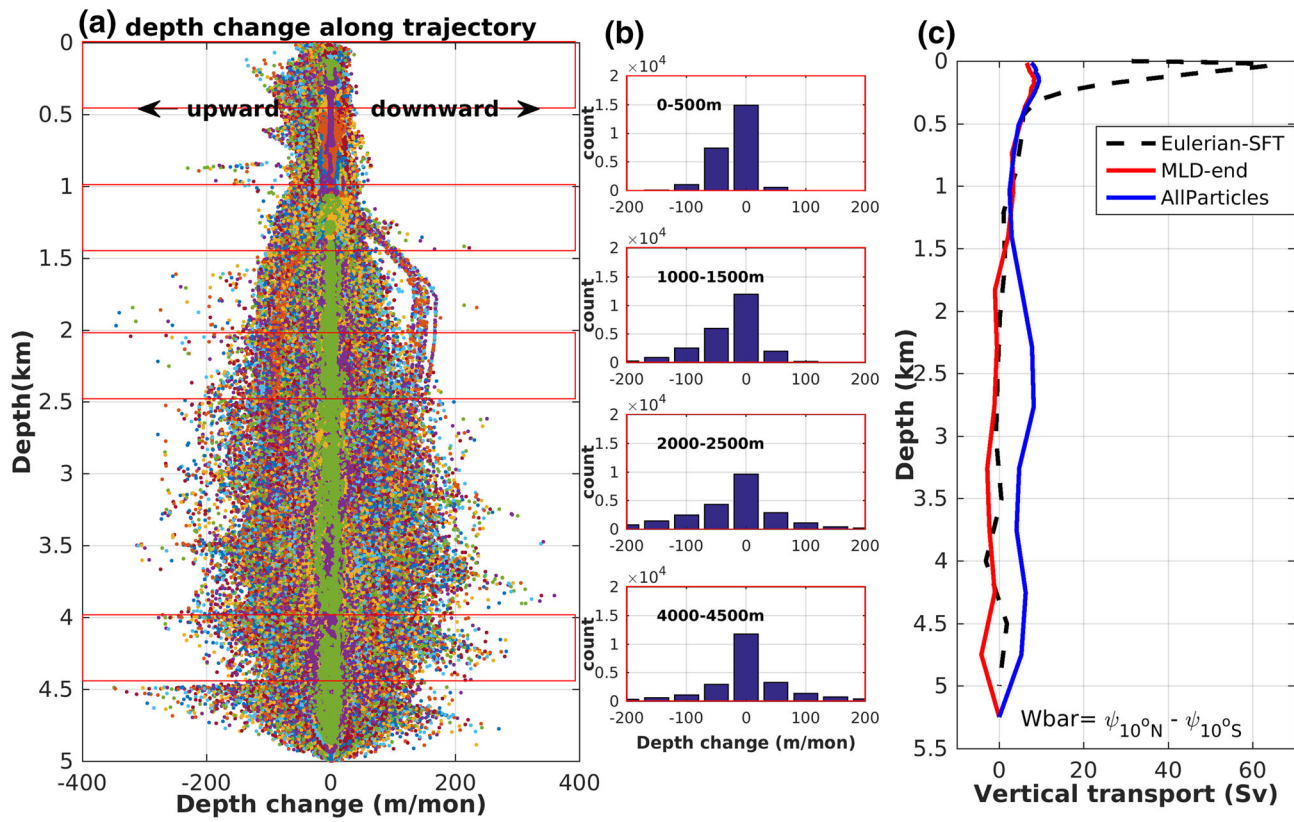


Figure 7. Depth changes as a function of depth along paleo-AABW parcels trajectories. (a) Scatterplot of depth changes (in meters per month, negative: upward; positive: downward) as a function of depth. (b) Particle distribution as a function of depth change, shown at various vertical layers as indicated by the boxes in Figure 7a. (c) Vertical transport over the tropical region 10°N to 10°S, derived from the corresponding stream functions.

definition, the MOC stream function differences for a given latitude band ($\Psi_{latn} - \Psi_{lats}$) represent the vertical transport of this region, with positive values indicating upward transport and negative values reflecting downward transport. For instance, over the latitude band of 10°S and 10°N, stream functions based on water parcels crossing the MLB and on all particles both estimate a noticeable upward water mass transport at shallow to intermediate depths (e.g., upper 1,500 m), with good agreement between them (Figure 7c). Compared with Eulerian-inferred results, these particles reproduce Eulerian-inferred vertical transports well at intermediate depths (i.e., 500–1,500 m), and only a fraction of transport over shallow depths. In particular, water parcels only represent a small part of upwelling transport over the top 500 m.

This efficient upwelling circulation over tropical regions during the early Eocene is favored by the continental geometry, compared with PI conditions. First, the three basins (Pacific, Atlantic and Indian) are well connected over the tropical regions by the opened Panama Strait, the wide Gibraltar Strait and the remains of the Tethys Sea. These well-connected ocean basins allow circum-circulation across all longitudes, in a similar way as the ACC under the present-day condition, despite with a weaker intensity, and at different latitude range. Second, the broad extension of the Pacific basin along the east-west direction over the tropics, 20% larger than the present day over most of the tropical latitudes, provides more space for accumulating wind-driven divergence at the surface (and shallow levels), and facilitates the strong upwelling on the east side of the basin. For the Atlantic basin, although the overall basin size is smaller than today, the basin width at 0–10°S (where numerous water parcels enter the thermocline) reaches up to 4,000 km, which is sufficient to permit upwelling over the eastern basin at this latitude band. The final geographical locations where water parcels enter the mixed layer are constrained to upwelling regions and can be inferred from the wind stress curl (Figures 5b and S6a). There are no significant differences in wind stress between the early Eocene and present-day conditions (Zhang et al., 2020). Therefore, the continental geometry differences are probably responsible for this efficient equatorial and tropical upwelling process.

This strong upwelling of deep water near the equator serves as a return path for paleo-AABW from the interior ocean to the surface mixed layer. In this sense, the tropical regions during the early Eocene are analogous to the present-day Southern Ocean, because both of them transport deep water upward and are essential for the closure of the overturning circulation. The role of Southern Ocean upwelling that is driven by strong westerlies across all longitudes in closing the present-day MOC has been highlighted by numerous studies (Anderson et al., 2009; Blanke et al., 2002; Garzoli & Matano, 2011; Marshall & Speer, 2012; Tamsitt et al., 2018; Wolfe & Cessi, 2014). Both observation data and numerical experiments confirm that the NADW is brought into the surface by the Southern Ocean upwelling through inter-hemisphere overturning circulation (Marshall & Speer, 2012). More directly, Lagrangian analysis and CFC tracer observation demonstrate the deepwater upwelling in the Southern Ocean through the ACC (Blanke et al., 2002; Rhein et al., 2015; Tamsitt et al., 2017). In the absence of such a route to the surface for paleo-AABW in the Eocene, equatorial and tropical upwelling provide the privileged return route to the surface. As such, the strong tropical upwelling of deep water during the early Eocene can play an analogous role to the present-day Southern Ocean upwelling.

4.2. Implications of Strong Tropical Upwelling on Global Carbon Cycle

The tropical upwelling during the early Eocene serves as an efficient return path for paleo-AABW and thus links the interior ocean to the surface ocean and eventually to the atmosphere. The potential efficiency of the upwelling process to affect the global carbon cycle has been well illustrated by the Pleistocene glacial cycles (Anderson et al., 2009; Burke & Robinson, 2012; Sigman & Boyle, 2000). Multiple processes operating among various reservoirs in the carbon system may likely be involved in contributing to the full amplitude of CO₂ variability during the last glacial-interglacial transition—up to 100 ppm as archived in the ice core (Barnola et al., 1987; Sigman & Boyle, 2000). The continental reservoir of organic carbon decreased during the glacial period mainly via two processes accompanied by the extension of glaciers at high latitudes: (1) degraded vegetation cover reduced biomass carbon (~15 ppm) and (2) exposure of sediments on continental shelves enhanced weathering. Nevertheless, terrestrial carbon is a small reservoir and may only be a modest source for glacial-interglacial CO₂ variation, especially considering the buffering effect of the ocean reservoir. For the ocean reservoir, dynamical carbon storage in the ocean associated with physico-chemical and biogeochemical processes in response to changes in oceanic chemical composition has been suggested to play an important role (François et al., 1997; Sigman & Boyle, 2000). Regarding physico-chemical processes, changes in CO₂ storage of the surface ocean due to cooler temperatures and high salinity may reduce atmospheric CO₂ by 23 ppm. Part of this reduction may be compensated by an associated weathering-induced alkalinity balance (e.g., 15–20 ppm), that is, temporary imbalances between input from weathering and output by the burial of biogenic calcium carbonate in the ocean sediment. Biogeochemical processes refer to the extraction of carbon from the surface ocean by biological production, allied with changes in the marine calcium carbonate budget. The availability of ocean nutrients in the low-latitude ocean, the key to this biogeochemical process, can regulate biological export production, which in turn determines the sequestration of inorganic carbon in the deep ocean by photosynthesis and the subsequent rain of organic carbon out of the upper ocean (Broecker, 1982; Sigman & Boyle, 2000). For instance, it has been estimated that a 30% increase in oceanic nutrients can decrease atmospheric CO₂ concentrations by 30–45 ppm (Sigman et al., 1998). More importantly, it has been demonstrated that increased nutrient utilization in the high-latitude Southern Ocean can also contribute to glacial CO₂ reduction (Knox & McElroy, 1984; Sarmiento & Toggweiler, 1984), which requires increased isolation of deepwater masses from the atmosphere (Köhler et al., 2005; Peacock et al., 2006; Sigman & Boyle, 2000; Watson & Naveira Garabato, 2006). The Southern Ocean plays a central role in regulating the glacial-interglacial variability of atmospheric CO₂ because deepwater masses outcrop in the Southern Ocean and exchange gases with the atmosphere (François et al., 1997; Sigman & Boyle, 2000). More recently, using biogenic opal data as an upwelling indicator, Anderson et al. (2009) proposed that a change in Southern Ocean upwelling circulation (ventilation of the deepwater masses) substantially alters the partitioning of CO₂ between the atmosphere and the deep sea. This potential link of changed ventilation in the Southern Ocean to the fluctuations of atmospheric CO₂ across glacial-interglacial cycles during the late Pleistocene has been further elaborated by recently available data arising from the development of novel methods (e.g., Burke & Robinson, 2012; Martínez-Botí et al., 2015). For instance, radiocarbon records from deep-sea corals have suggested that enhanced ventilation in the Southern Ocean since the last Glacial Maximum (21 ka) contributed to an increase in atmospheric CO₂ concentration during the last

deglaciation (Anderson et al., 2009; Burke & Robinson, 2012). Recent boron isotope data, as a more direct tracer of oceanic CO₂ outgassing, further suggest that strengthened upwelling caused a leakage of oceanic carbon over the Southern Ocean, driving the increasing atmospheric CO₂ over the course of the last deglaciation (Martínez-Botí et al., 2015). Such non-negligible changes, caused by the variation of the Southern Ocean upwelling over the late Pleistocene glacial cycles, demonstrate that upwelling dynamics can significantly change the global carbon distribution.

During the Eocene, the low-latitudinal geographical locations of the upwelling process and associated high temperature can reinforce the influence of upwelling on the global carbon cycle by inducing physico-chemical and biogeochemical processes. From the physico-chemical perspective, the solubility of greenhouse gases is a strong inverse function of seawater temperature. The higher temperatures over upwelling regions may lead to more complete degassing of upwelled water and promote an effective solubility pump of greenhouse gases from the abyssal ocean into the atmosphere, although the absolute gas content hold in water can be reduced by the overall warm Eocene environment. Hypothetically, this intensified solubility of upwelling water can transfer a tremendous amount of carbon from the abyssal ocean to the atmosphere, via efficient exposure of carbon-rich deep water to the active surface mixed layer. From a biogeochemical perspective, strong upwelling theoretically brings nutrients up to the upper ocean and enhances marine primary productivity. However, biogenic silica accumulation rates, as an indicator of biological productivity, in the equatorial zone of the Pacific during the Eocene have been found to be lower than in the Neogene (Moore et al., 2004, 2008). Given the complex processes involved in transforming biological production into preserved biogenic sediment (especially for such deep geological time), several factors may explain this discrepancy between expected high primary productivity and low sedimentation rates (Olivarez Lyle & Lyle, 2005, 2006). First, in addition to primary production, complicated secondary processes influence the settling flux and final burial of organic matter on the seafloor as sediment deposits, which can lead to substantial uncertainties in using biogenic silica as a proxy for biological production for such an ancient time period (e.g., Sigman et al., 1998; Sigman & Boyle, 2000). For instance, the extremely warm Eocene environment may substantially enhance the basal metabolic rate of the oceanic biota in deeper waters and accelerate nutrient recycling, which can reduce burial on the seafloor, thus reducing the biogenic silica accumulation rate (Olivarez Lyle & Lyle, 2005, 2006). Meanwhile, increase in the dissolved nutrient concentrations of ocean waters below the photic zone may support high respiration rates and consume the primary production (as mentioned by Moore et al., 2008; Piper & Calvert, 2009). Second, the preservation of sediment is also an important issue (Moore et al., 2008), which can be affected by an erosion process or the secondary dissolution due to a totally different physico-chemical environment (Pichon et al., 1992). In particular, the Eocene is at the base of most sediment cores, and fewer sediment core data are available for the Eocene period than for the later periods (e.g., Oligocene). Potentially, strongly connected tropical pathways may allow enhanced bottom currents that further modify sediment deposition. These large uncertainties may explain the discrepancies between the low silica accumulation rates and the expected enhanced biological pump from the upwelling found in our study.

The potential sources of this abyssal ocean carbon are also subject to substantial uncertainty, although they have been explored from different perspectives (Cui et al., 2011; Sexton et al., 2011). The first hypothetical origin of this Eocene carbon input is oceanic dissolved carbon sequestered in the abyssal ocean during previous geological times (Sexton et al., 2011), perhaps with a similar process occurring during the younger intervals of Earth history as during the Pleistocene glacial cycles (Anderson et al., 2009; Burke & Robinson, 2012). The second hypothesis attributes this Eocene carbon input to the releases of carbon from buried sediments (Nicolo et al., 2007; Panchuk et al., 2008). However, here, we could not pin down which of the above mentioned sources would be more plausible yet, and the exact magnitude of these processes remains to be determined from more data on the total carbon reservoirs in the deep ocean.

Overall, despite uncertainties in biogeochemical processes and possible carbon sources, our results, from the oceanic dynamics perspective, demonstrate the efficient communication between the abyssal ocean and the surface mixed ocean, which could effectively influence the related carbon exchange and perhaps regulate climate evolution during the Eocene.

5. Conclusions

Coupled model simulations of the Eocene suggest a very intense overturning originating in the Southern Ocean, and no deepwater formation in the Northern Hemisphere. Here, we used the Lagrangian analysis tool Ariane releasing thousands of particles from the lower limb of this MOC at latitude 60°S to follow the paleo-AABW masses leaving the Southern Ocean. Their trajectories were subsequently analyzed to trace the fates of this northward flowing bottom and deep waters. With a good representation of the northward flowing deepwater transports at the initial section, the Lagrangian analysis revealed two fates for the paleo-AABW. The majority of paleo-AABW returns to the Southern Ocean either through the initial section (~43%) as part of recirculation or through the section above the initial section (~31%), and >25% eventually enters the surface ocean by crossing the base of the mixed layer. Nearly half of the latter water parcels (9 Sv) enters the surface ocean in tropical regions (30°S to 30°N). This is quite different from the present-day situation, in which most of the NADW comes out into the surface ocean in the Southern Ocean, and AABW comes out in the region of 40°S.

Most of these water parcels experience negative density transformation before reaching the surface mixed layer. This density transformation mainly occurs in the upper 500 m of the tropical upwelling regions, which is accompanied by an effective upward overturning. The spatial pattern of this negative density transformation is consistent with wind-driven Ekman pumping that is favored by the Eocene continental geometry, including the widely extended Pacific basin and the presence of tropical gateways (permitting substantial inter-basin connection in the tropics).

Our results indicate that the strong tropical upwelling during the early Eocene—resembling the present-day Southern Ocean upwelling for the NADW, but occurring at much higher temperature—provided an efficient pathway from the deep ocean to the surface ocean, which may promote carbon release from the deep ocean through physico-chemical and biogeochemical processes. The exposure of the carbon-rich deep water in upwelling regions can promote the solubility pump of greenhouse gases from the abyssal ocean into the atmosphere, although the absolute gas content of seawater may be reduced in a warm Eocene environment. Meanwhile, upwelling can modify the nutrients distribution, which may change biological export production by triggering changes in biogeochemical processes. These physico-chemical and biogeochemical responses related to upwelling potentially facilitate carbon release from the abyssal ocean to the surface ocean (and eventually to the atmosphere), which perhaps in turn affected other processes of the carbon cycle and climate evolution during the Eocene. These speculations probably deserve a more detailed analysis with a full carbon cycle model for this particularly warm period of the Earth climate.

Data Availability Statement

The Lagrangian experiment data of this study have been archived in the PANGAEA database (<https://doi.pangaea.de/10.1594/PANGAEA.911376>).

Acknowledgments

We acknowledge invaluable contributions from anonymous reviewers and pertinent suggestions from the Editor that have greatly clarified and improved the manuscript. We would like to thank Camille Lique for initiating this project and discussions in the early stage of the study. The IPSL-CM5A2 model simulations were provided by Yannick Donnadieu (CEREGE), Jean-Baptiste Ladant, and Pierre Sepulchre (LSCE). This research received funding from the French National Research Agency (ANR) under the “Programme d’Investissements d’Avenir” ISblue (ANR-17-EURE-0015) and LabexMER (ANR-10-LABX-19) for the COPS project. Additional funding was provided by IFREMER and the “Université Bretagne Loire” for Yurui Zhang’s postdoctoral fellowship.

References

- Anderson, R. F., Ali, S., Bradtmiller, L. I., Nielsen, S. H. H., Fleisher, M. Q., Anderson, B. E., & Burckle, L. H. (2009). Wind-driven upwelling in the Southern Ocean and the deglacial rise in atmospheric CO₂. *Science*, 323(5920), 1443–1448. <https://doi.org/10.1126/science.1167441>
- Baatsen, M., von der Heydt, A. S., Huber, M., Kliphuis, M. A., Bijl, P. K., Sluijs, A., & Dijkstra, H. A. (2018). Equilibrium state and sensitivity of the simulated middle-to-late Eocene climate. *Climate of the Past Discussions*, 1–49. <https://doi.org/10.5194/cp-2018-43>
- Barnola, J. M., Raynaud, D., Korotkevich, Y. S., & Lorius, C. (1987). Vostok ice core provides 160,000-year record of atmospheric CO₂. *Nature*, 329(6138), 408–414. <https://doi.org/10.1038/329408a0>
- Blanke, B., Arhan, M., Madec, G., & Roche, S. (1999). Warm water paths in the equatorial Atlantic as diagnosed with a general circulation model. *Journal of Physical Oceanography*, 29(11), 2753–2768. [https://doi.org/10.1175/1520-0485\(1999\)029<2753:WWPITE>2.0.CO;2](https://doi.org/10.1175/1520-0485(1999)029<2753:WWPITE>2.0.CO;2)
- Blanke, B., Arhan, M., & Speich, S. (2006). Salinity changes along the upper limb of the Atlantic thermohaline circulation. *Geophysical Research Letters*, 33, L06609. <https://doi.org/10.1029/2005GL024938>
- Blanke, B., & Raynaud, S. (1997). Kinematics of the Pacific equatorial undercurrent: An Eulerian and Lagrangian approach from GCM results. *Journal of Physical Oceanography*, 27(6), 1038–1053. [https://doi.org/10.1175/1520-0485\(1997\)027<1038:KOTPEU>2.0.CO;2](https://doi.org/10.1175/1520-0485(1997)027<1038:KOTPEU>2.0.CO;2)
- Blanke, B., Speich, S., Madec, G., & Maugé, R. (2002). A global diagnostic of interior ocean ventilation. *Geophysical Research Letters*, 29(8), 1267. <https://doi.org/10.1029/2001GL013727>
- Bower, A., Lozier, S., Biastoch, A., Drouin, K., Foukal, N., Furey, H., et al. (2019). Lagrangian views of the pathways of the Atlantic Meridional Overturning Circulation. *Journal of Geophysical Research: Oceans*, 124, 5313–5335. <https://doi.org/10.1029/2019JC015014>
- Breecker, D. O., Sharp, Z. D., & McFadden, L. D. (2010). Atmospheric CO₂ concentrations during ancient greenhouse climates were similar to those predicted for A.D. 2100. *Proceedings of the National Academy of Sciences*, 107(2), 576–580. <https://doi.org/10.1073/pnas.0902323106>

- Broecker, W. S. (1982). Ocean chemistry during glacial time. *Geochimica et Cosmochimica Acta*, 46(10), 1689–1705. [https://doi.org/10.1016/0016-7037\(82\)90110-7](https://doi.org/10.1016/0016-7037(82)90110-7)
- Broecker, W., & Barker, S. (2007). A 190‰ drop in atmosphere's $\Delta^{14}\text{C}$ during the “Mystery Interval” (17.5 to 14.5 kyr). *Earth and Planetary Science Letters*, 256(1–2), 90–99. <https://doi.org/10.1016/j.epsl.2007.01.015>
- Bullister, J. L., Rhein, M., & Mauritzen, C. (2013). Chapter 10—Deepwater formation. In G. Siedler, S. M. Griffies, J. Gould, J. A. Church (Eds.), *Ocean circulation and climate* (Vol. 103, pp. 227–253). Academic Press. <https://doi.org/10.1016/B978-0-12-391851-2.00010-6>
- Burke, A., & Robinson, L. F. (2012). The Southern Ocean's role in carbon exchange during the last deglaciation. *Science*, 335(6068), 557–561. <https://doi.org/10.1126/science.1208163>
- Contoux, C., Jost, A., Ramstein, G., Sepulchre, P., Krinner, G., & Schuster, M. (2013). Megalake Chad impact on climate and vegetation during the late Pliocene and the mid-Holocene. *Climate of the Past*, 9(4), 1417–1430. <https://doi.org/10.5194/cp-9-1417-2013>
- Cramer, B. S., Miller, K. G., Barrett, P. J., & Wright, J. D. (2011). Late Cretaceous–Neogene trends in deep ocean temperature and continental ice volume: Reconciling records of benthic foraminiferal geochemistry ($\delta^{18}\text{O}$ and Mg/Ca) with sea level history. *Journal of Geophysical Research*, 116, C12023. <https://doi.org/10.1029/2011JC007255>
- Cramwinckel, M. J., Huber, M., Kocken, I. J., Agnini, C., Bijl, P. K., Bohaty, S. M., et al. (2018). Synchronous tropical and polar temperature evolution in the Eocene. *Nature*, 559(7714), 382–386. <https://doi.org/10.1038/s41586-018-0272-2>
- Cui, Y., Kump, L. R., Ridgwell, A. J., Charles, A. J., Junium, C. K., Diefendorf, A. F., et al. (2011). Slow release of fossil carbon during the Palaeocene–Eocene Thermal Maximum. *Nature Geoscience*, 4(7), 481–485. <https://doi.org/10.1038/ngeo1179>
- Davies, A., Hunter, S. J., Gréselle, B., Haywood, A. M., & Robson, C. (2019). Evidence for seasonality in early Eocene high latitude sea-surface temperatures. *Earth and Planetary Science Letters*, 519, 274–283. <https://doi.org/10.1016/j.epsl.2019.05.025>
- DeConto, R. M., Galeotti, S., Pagani, M., Tracy, D., Schaefer, K., Zhang, T., et al. (2012). Past extreme warming events linked to massive carbon release from thawing permafrost. *Nature*, 484(7392), 87–91. <https://doi.org/10.1038/nature10929>
- Döös, K. (1995). Inter-ocean exchange of water masses. *Journal of Geophysical Research*, 100(C7), 13,499–13,514. <https://doi.org/10.1029/95JC00337>
- Döös, K., Nycander, J., & Coward, A. C. (2008). Lagrangian decomposition of the Deacon cell. *Journal of Geophysical Research*, 113, C07028. <https://doi.org/10.1029/2007JC004351>
- Döös, K., & Webb, D. J. (1994). The Deacon cell and the other meridional cells of the Southern Ocean. *Journal of Physical Oceanography*, 24(2), 429–442. [https://doi.org/10.1175/1520-0485\(1994\)024<0429:TDCATO>2.0.CO;2](https://doi.org/10.1175/1520-0485(1994)024<0429:TDCATO>2.0.CO;2)
- Dufresne, J.-L., Foujols, M.-A., Denvil, S., Caubel, A., Marti, O., Aumont, O., et al. (2013). Climate change projections using the IPSL-CM5 Earth System Model: From CMIP3 to CMIP5. *Climate Dynamics*, 40(9–10), 2123–2165. <https://doi.org/10.1007/s00382-012-1636-1>
- Dunkley Jones, T., Lunt, D. J., Schmidt, D. N., Ridgwell, A., Sluijs, A., Valdes, P. J., & Maslin, M. (2013). Climate model and proxy data constraints on ocean warming across the Paleocene–Eocene Thermal Maximum. *Earth-Science Reviews*, 125, 123–145. <https://doi.org/10.1016/j.earscirev.2013.07.004>
- Ferreira, D., Cessi, P., Coxall, H. K., de Boer, A., Dijkstra, H. A., Drijfhout, S. S., et al. (2018). Atlantic-Pacific asymmetry in deep water formation. *Annual Review of Earth and Planetary Sciences*, 46(1), 327–352. <https://doi.org/10.1146/annurev-earth-082517-010045>
- Foster, G. L., Royer, D. L., & Lunt, D. J. (2017). Future climate forcing potentially without precedent in the last 420 million years. *Nature Communications*, 8(1), 14845. <https://doi.org/10.1038/ncomms14845>
- François, R., Altabet, M. A., Yu, E.-F., Sigman, D. M., Bacon, M. P., Frank, M., et al. (1997). Contribution of Southern Ocean surface-water stratification to low atmospheric CO_2 concentrations during the last glacial period. *Nature*, 389(6654), 929–935. <https://doi.org/10.1038/40073>
- Ganachaud, A., & Wunsch, C. (2000). Improved estimates of global ocean circulation, heat transport and mixing from hydrographic data. *Nature*, 408(6811), 453–457. <https://doi.org/10.1038/35044048>
- Garzoli, S. L., & Matano, R. (2011). The South Atlantic and the Atlantic Meridional Overturning Circulation. *Deep Sea Research Part II: Topical Studies in Oceanography*, 58(17–18), 1837–1847. <https://doi.org/10.1016/j.dsr2.2010.10.063>
- Gent, P. R., & McWilliams, J. C. (1990). Isopycnal mixing in ocean circulation models. *Journal of Physical Oceanography*, 20(1), 150–155. [https://doi.org/10.1175/1520-0485\(1990\)020<0150:imiocm>2.0.co;2](https://doi.org/10.1175/1520-0485(1990)020<0150:imiocm>2.0.co;2)
- Gordon, A. L. (1971). Oceanography of Antarctic Waters. In J. L. Reid (Ed.), *Antarctic Oceanology I*. <https://doi.org/10.1029/AR015p0169>
- Green, J. A. M., & Huber, M. (2013). Tidal dissipation in the early Eocene and implications for ocean mixing: Eocene tides. *Geophysical Research Letters*, 40, 2707–2713. <https://doi.org/10.1002/grl.50510>
- Griffa, A., Kirwan, A. D. J., Mariano, A. J., Ozgokmen, T., & Rossby, H. T. (Eds.) (2007). *Lagrangian analysis and prediction of coastal and ocean dynamics*. Cambridge: Cambridge University Press.
- Herold, N., Buzan, J., Seton, M., Goldner, A., Green, J. A. M., Müller, R. D., et al. (2014). A suite of early Eocene (~55 Ma) climate model boundary conditions. *Geoscientific Model Development*, 7(5), 2077–2090. <https://doi.org/10.5194/gmd-7-2077-2014>
- Ho, S. L., & Laepple, T. (2016). Flat meridional temperature gradient in the early Eocene in the subsurface rather than surface ocean. *Nature Geoscience*, 9(8), 606–610. <https://doi.org/10.1038/ngeo2763>
- Hollis, C. J., Dunkley Jones, T., Anagnostou, E., Bijl, P. K., Cramwinckel, M. J., Cui, Y., et al. (2019). The DeepMIP contribution to PMIP4: Methodologies for selection, compilation and analysis of latest Paleocene and early Eocene climate proxy data, incorporating Version 0.1 of the DeepMIP database. *Geoscientific Model Development*, 12(7), 3149–3206. <https://doi.org/10.5194/gmd-12-3149-2019>
- Hourdin, F., Grandpeix, J.-Y., Rio, C., Bony, S., Jam, A., Cheruy, F., et al. (2013). LMDZ5B: The atmospheric component of the IPSL climate model with revisited parameterizations for clouds and convection. *Climate Dynamics*, 40(9–10), 2193–2222. <https://doi.org/10.1007/s00382-012-1343-y>
- Huber, M. (2008). A hotter greenhouse? *Science*, 321(5887), 353–354. <https://doi.org/10.1126/science.1161170>
- Huber, M., & Caballero, R. (2011). The early Eocene equable climate problem revisited. *Climate of the Past*, 7(2), 603–633. <https://doi.org/10.5194/cp-7-603-2011>
- Hutchinson, D. K., de Boer, A. M., Coxall, H. K., Caballero, R., Nilsson, J., & Baatsen, M. (2018). Climate sensitivity and meridional overturning circulation in the late Eocene using GFDL CM2.1. *Climate of the Past*, 14(6), 789–810. <https://doi.org/10.5194/cp-14-789-2018>
- Iudicone, D., Lacorata, G., Rupolo, V., Santoleri, R., & Vulpiani, A. (2002). Sensitivity of numerical tracer trajectories to uncertainties in OGCM velocity fields. *Ocean Modelling*, 4(3–4), 313–325. [https://doi.org/10.1016/S1463-5003\(02\)00006-9](https://doi.org/10.1016/S1463-5003(02)00006-9)
- John, E. H., Pearson, P. N., Coxall, H. K., Birch, H., Wade, B. S., & Foster, G. L. (2013). Warm ocean processes and carbon cycling in the Eocene. *Philosophical Transactions of the Royal Society A: Mathematical, Physical and Engineering Sciences*, 371(2001), 20130099. <https://doi.org/10.1098/rsta.2013.0099>
- John, E. H., Wilson, J. D., Pearson, P. N., & Ridgwell, A. (2014). Temperature-dependent remineralization and carbon cycling in the warm Eocene oceans. *Palaeogeography, Palaeoclimatology, Palaeoecology*, 413, 158–166. <https://doi.org/10.1016/j.palaeo.2014.05.019>

- Johnson, G. C. (2008). Quantifying Antarctic Bottom Water and North Atlantic Deep Water volumes. *Journal of Geophysical Research*, *113*, C05027. <https://doi.org/10.1029/2007JC004477>
- Kageyama, M., Braconnot, P., Bopp, L., Caubel, A., Foujols, M.-A., Guilyardi, E., et al. (2013). Mid-Holocene and Last Glacial Maximum climate simulations with the IPSL model—Part I: Comparing IPSL_CM5A to IPSL_CM4. *Climate Dynamics*, *40*(9–10), 2447–2468. <https://doi.org/10.1007/s00382-012-1488-8>
- Kennedy-Asser, A. T., Lunt, D. J., Valdes, P. J., Ladant, J.-B., Frieling, J., & Laurentino, V. (2020). Changes in the high-latitude Southern Hemisphere through the Eocene–Oligocene transition: A model–data comparison. *Climate of the Past*, *16*(2), 555–573. <https://doi.org/10.5194/cp-16-555-2020>
- Knox, F., & McElroy, M. B. (1984). Changes in atmospheric CO₂: Influence of the marine biota at high latitude. *Journal of Geophysical Research*, *89*(D3), 4629–4637. <https://doi.org/10.1029/JD089iD03p04629>
- Köhler, P., Fischer, H., Munhoven, G., & Zeebe, R. E. (2005). Quantitative interpretation of atmospheric carbon records over the last glacial termination. *Global Biogeochemical Cycles*, *19*, GB4020. <https://doi.org/10.1029/2004GB002345>
- Kuhlbrodt, T., Griesel, A., Montoya, M., Levermann, A., Hofmann, M., & Rahmstorf, S. (2007). On the driving processes of the Atlantic Meridional Overturning Circulation. *Reviews of Geophysics*, *45*, RG2001. <https://doi.org/10.1029/2004RG000166>
- Kurtz, A. C., Kump, L. R., Arthur, M. A., Zachos, J. C., & Paytan, A. (2003). Early Cenozoic decoupling of the global carbon and sulfur cycles. *Paleoceanography*, *18*(4), 1090. <https://doi.org/10.1029/2003PA000908>
- Ladant, J.-B., Donnadieu, Y., Lefebvre, V., & Dumas, C. (2014). The respective role of atmospheric carbon dioxide and orbital parameters on ice sheet evolution at the Eocene–Oligocene transition: Ice sheet evolution at the EOT. *Paleoceanography*, *29*, 810–823. <https://doi.org/10.1002/2013PA002593>
- Liu, L. L., & Huang, R. X. (2012). The global subduction/obduction rates: Their interannual and decadal variability. *Journal of Climate*, *25*(4), 1096–1115. <https://doi.org/10.1175/2011JCLI4228.1>
- Lumpkin, R., & Speer, K. (2007). Global ocean meridional overturning. *Journal of Physical Oceanography*, *37*(10), 2550–2562. <https://doi.org/10.1175/JPO3130.1>
- Lunt, D. J., Bragg, F., Chan, W.-L., Hutchinson, D. K., Ladant, J.-B., Niezgodzki, I., et al. (2020). DeepMIP: Model intercomparison of early Eocene climatic optimum (EECO) large-scale climate features and comparison with proxy data. *Climate of the Past*. <https://doi.org/10.5194/cp-2019-149>
- Lunt, D. J., Dunkley Jones, T., Heinemann, M., Huber, M., LeGrande, A., Winguth, A., et al. (2012). A model–data comparison for a multi-model ensemble of early Eocene atmosphere–ocean simulations: EoMIP. *Climate of the Past*, *8*(5), 1717–1736. <https://doi.org/10.5194/cp-8-1717-2012>
- Lunt, D. J., Huber, M., Anagnostou, E., Baatsen, M. L. J., Caballero, R., DeConto, R., et al. (2017). The DeepMIP contribution to PMIP4: Experimental design for model simulations of the EECO, PETM, and pre-PETM (Version 1.0). *Geoscientific Model Development*, *10*(2), 889–901. <https://doi.org/10.5194/gmd-10-889-2017>
- Lunt, D. J., Valdes, P. J., Jones, T. D., Ridgwell, A., Haywood, A. M., Schmidt, D. N., et al. (2010). CO₂-driven ocean circulation changes as an amplifier of Paleocene–Eocene Thermal Maximum hydrate destabilization. *Geology*, *38*(10), 875–878. <https://doi.org/10.1130/G31184.1>
- Macdonald, A. M., & Wunsch, C. (1996). An estimate of global ocean circulation and heat fluxes. *Nature*, *382*(6590), 436–439. <https://doi.org/10.1038/382436a0>
- Maffre, P., Ladant, J.-B., Donnadieu, Y., Sepulchre, P., & Godd eris, Y. (2018). The influence of orography on modern ocean circulation. *Climate Dynamics*, *50*(3–4), 1277–1289. <https://doi.org/10.1007/s00382-017-3683-0>
- Marshall, J., & Speer, K. (2012). Closure of the meridional overturning circulation through Southern Ocean upwelling. *Nature Geoscience*, *5*(3), 171–180. <https://doi.org/10.1038/ngeo1391>
- Martinez-Bot , M. A., Marino, G., Foster, G. L., Ziveri, P., Henahan, M. J., Rae, J. W. B., et al. (2015). Boron isotope evidence for oceanic carbon dioxide leakage during the last deglaciation. *Nature*, *518*(7538), 219–222. <https://doi.org/10.1038/nature14155>
- Moore, T. C., Backman, J., Raffi, I., Nigrini, C., Sanfilippo, A., P alike, H., & Lyle, M. (2004). Paleogene tropical Pacific: Clues to circulation, productivity, and plate motion. *Paleoceanography*, *19*, PA3013. <https://doi.org/10.1029/2003PA000998>
- Moore, T. C., Jarrard, R. D., Olivarez Lyle, A., & Lyle, M. (2008). Eocene biogenic silica accumulation rates at the Pacific equatorial divergence zone: Eocene biogenic silica. *Paleoceanography*, *23*, PA2202. <https://doi.org/10.1029/2007PA001514>
- Munk, W. H. (1966). Abyssal recipes. *Deep-Sea Research*, *13*, 707–730.
- Nicolo, M. J., Dickens, G. R., Hollis, C. J., & Zachos, J. C. (2007). Multiple early Eocene hyperthermals: Their sedimentary expression on the New Zealand continental margin and in the deep sea. *Geology*, *35*(8), 699–702. <https://doi.org/10.1130/G23648A.1>
- Nof, D. (2000). Does the wind control the import and export of the South Atlantic? *Journal of Physical Oceanography*, *30*, 2650–2667.
- Nof, D., & Gorder, S. V. (2003). Did an open Panama isthmus correspond to an invasion of Pacific water into the Atlantic? *Journal of Physical Oceanography*, *33*, 1324–1336.
- Olivarez Lyle, A., & Lyle, M. (2005). Organic carbon and barium in Eocene sediments: Possible controls on nutrient recycling in the Eocene equatorial Pacific Ocean. *Proc. Ocean Drill. Program Sci. Results*, *199*, 1–33.
- Olivarez Lyle, A., & Lyle, M. (2006). Missing organic carbon in Eocene marine sediments: Is metabolism the biological feedback that maintains end-member climates? *Paleoceanography*, *21*, PA2007. <https://doi.org/10.1029/2005PA001230>
- Orsi, A. H., Johnson, G. C., & Bullister, J. L. (1999). Circulation, mixing, and production of Antarctic Bottom Water. *Progress in Oceanography*, *43*(1), 55–109. [https://doi.org/10.1016/S0079-6611\(99\)00004-X](https://doi.org/10.1016/S0079-6611(99)00004-X)
- Pagani, M., Arthur, M. A., & Freeman, K. H. (1999). Miocene evolution of atmospheric carbon dioxide. *Paleoceanography*, *14*(3), 273–292. <https://doi.org/10.1029/1999PA900006>
- Panchuk, K., Ridgwell, A., & Kump, L. R. (2008). Sedimentary response to Paleocene–Eocene Thermal Maximum carbon release: A model–data comparison. *Geology*, *36*(4), 315–318. <https://doi.org/10.1130/G24474A.1>
- Peacock, S., Lane, E., & Restrepo, J. M. (2006). A possible sequence of events for the generalized glacial–interglacial cycle. *Global Biogeochemical Cycles*, *20*, GB2010. <https://doi.org/10.1029/2005GB002448>
- Pearson, P. N., & Palmer, M. R. (2000). Atmospheric carbon dioxide concentrations over the past 60 million years. *Nature*, *406*(6797), 695–699. <https://doi.org/10.1038/35021000>
- Pichon, J. J., Bareille, G., Labracherie, M., Labeysrie, L. D., Baudrimont, A., & Turon, J. L. (1992). Quantification of the biogenic silica dissolution in Southern Ocean sediments. *Quaternary Research*, *37*(3), 361–378. [https://doi.org/10.1016/0033-5894\(92\)90073-R](https://doi.org/10.1016/0033-5894(92)90073-R)
- Piper, D. Z., & Calvert, S. E. (2009). A marine biogeochemical perspective on black shale deposition. *Earth-Science Reviews*, *95*(1–2), 63–96. <https://doi.org/10.1016/j.earscirev.2009.03.001>

- Qin, X., van Sebille, E., & Sen Gupta, A. (2014). Quantification of errors induced by temporal resolution on Lagrangian particles in an eddy-resolving model. *Ocean Modelling*, *76*, 20–30. <https://doi.org/10.1016/j.ocemod.2014.02.002>
- Rhein, M., Kieke, D., & Steinfeldt, R. (2015). Advection of North Atlantic Deep Water from the Labrador Sea to the Southern Hemisphere. *Journal of Geophysical Research: Oceans*, *120*, 2471–2487. <https://doi.org/10.1002/2014JC010605>
- Rimaud, J., Speich, S., Blanke, B., & Grima, N. (2012). The exchange of intermediate water in the southeast Atlantic: Water mass transformations diagnosed from the Lagrangian analysis of a regional ocean model: AAIW in the Southeast Atlantic. *Journal of Geophysical Research*, *117*, C08034. <https://doi.org/10.1029/2012JC008059>
- Sarmiento, J. L., & Toggweiler, J. R. (1984). A new model for the role of the oceans in determining atmospheric pCO₂. *Nature*, *308*(12), 621–624.
- Schmittner, A., Silva, T. A. M., Fraedrich, K., Kirk, E., & Lunkeit, F. (2011). Effects of mountains and ice sheets on global ocean circulation. *Journal of Climate*, *24*(11), 2814–2829. <https://doi.org/10.1175/2010JCLI3982.1>
- Sepulchre, P., Arsouze, T., Donnadieu, Y., Dutay, J.-C., Jaramillo, C., Le Bras, J., et al. (2014). Consequences of shoaling of the Central American Seaway determined from modeling Nd isotopes. *Paleoceanography*, *29*, 176–189. <https://doi.org/10.1002/2013PA002501>
- Sepulchre, P., Caubel, A., Ladant, J.-B., Bopp, L., Boucher, O., Braconnot, P., et al. (2020). IPSL-CM5A2. An Earth system model designed for long simulations of past and future climates. *Geoscientific Model Development*, *13*(7), 3011–3053. <https://doi.org/10.5194/gmd-13-3011-2020>
- Sexton, P. F., Norris, R. D., Wilson, P. A., Palike, H., Westerhold, T., Röhl, U., et al. (2011). Eocene global warming events driven by ventilation of oceanic dissolved organic carbon. *Nature*, *471*(7338), 349–352. <https://doi.org/10.1038/nature09826>
- Sigman, D. M., & Boyle, E. A. (2000). Glacial/interglacial variations in atmospheric carbon dioxide. *Nature*, *407*(6806), 859–869. <https://doi.org/10.1038/35038000>
- Sigman, D. M., McCorkle, D. C., & Martin, W. R. (1998). The calcite lysocline as a constraint on glacial/interglacial low-latitude production changes. *Global Biogeochemical Cycles*, *12*(3), 409–427. <https://doi.org/10.1029/98GB01184>
- Speich, S., Blanke, B., & Madec, G. (2001). Warm and cold water routes of an O.G.C.M. thermohaline conveyor belt. *Geophysical Research Letters*, *28*(2), 311–314. <https://doi.org/10.1029/2000GL011748>
- Srokosz, M., Baringer, M., Bryden, H., Cunningham, S., Delworth, T., Lozier, S., et al. (2012). Past, present, and future changes in the Atlantic Meridional Overturning Circulation. *Bulletin of the American Meteorological Society*, *93*(11), 1663–1676. <https://doi.org/10.1175/BAMS-D-11-00151.1>
- Tamsitt, V., Abernathy, R. P., Mazloff, M. R., Wang, J., & Talley, L. D. (2018). Transformation of deep water masses along Lagrangian upwelling pathways in the Southern Ocean: Southern Ocean upwelling transformation. *Journal of Geophysical Research: Oceans*, *123*, 1994–2017. <https://doi.org/10.1002/2017JC013409>
- Tamsitt, V., Drake, H., Morrison, A. K., Talley, L. D., Dufour, C. O., Gray, A. R., et al. (2017). Spiraling pathways of global deep waters to the surface of the Southern Ocean. *Nature Communications*, *8*(1), 172. <https://doi.org/10.1038/s41467-017-00197-0>
- Tan, N., Contoux, C., Ramstein, G., Sun, Y., Dumas, C., Sepulchre, P., & Guo, Z. (2020). Modeling a modern-like pCO₂ warm period (Marine Isotope Stage KM5c) with two versions of an Institut Pierre Simon Laplace atmosphere–ocean coupled general circulation model. *Climate of the Past*, *16*(1), 1–16. <https://doi.org/10.5194/cp-16-1-2020>
- Tan, N., Ladant, J.-B., Ramstein, G., Dumas, C., Bachem, P., & Jansen, E. (2018). Dynamic Greenland ice sheet driven by pCO₂ variations across the Pliocene Pleistocene transition. *Nature Communications*, *9*(1), 4755. <https://doi.org/10.1038/s41467-018-07206-w>
- Tan, N., Ramstein, G., Dumas, C., Contoux, C., Ladant, J.-B., Sepulchre, P., et al. (2017). Exploring the MIS M2 glaciation occurring during a warm and high atmospheric CO₂ Pliocene background climate. *Earth and Planetary Science Letters*, *472*, 266–276. <https://doi.org/10.1016/j.epsl.2017.04.050>
- Thomas, D. J., Bralower, T. J., & Jones, C. E. (2003). Neodymium isotopic reconstruction of late Paleocene–early Eocene thermohaline circulation. *Earth and Planetary Science Letters*, *209*(3–4), 309–322. [https://doi.org/10.1016/s0012-821x\(03\)00096-7](https://doi.org/10.1016/s0012-821x(03)00096-7)
- Thomas, D. J., Korty, R., Huber, M., Schubert, J. A., & Haines, B. (2014). Nd isotopic structure of the Pacific Ocean 70–30 Ma and numerical evidence for vigorous ocean circulation and ocean heat transport in a greenhouse world. *Paleoceanography*, *29*, 454–469. <https://doi.org/10.1002/2013PA002535>
- Toggweiler, J. R., Russell, J. L., & Carson, S. R. (2006). Midlatitude westerlies, atmospheric CO₂, and climate change during the ice ages. *Paleoceanography*, *21*, PA2005. <https://doi.org/10.1029/2005PA001154>
- Toggweiler, J. R., & Samuels, B. (1995). Effect of drake passage on the global thermohaline circulation. *Deep Sea Research Part I: Oceanographic Research Papers*, *42*(4), 477–500. [https://doi.org/10.1016/0967-0637\(95\)00012-U](https://doi.org/10.1016/0967-0637(95)00012-U)
- Toggweiler, J. R., & Samuels, B. (1998). On the ocean's large-scale circulation near the limit of no vertical mixing. *Journal of Physical Oceanography*, *28*(9), 1832–1852. [https://doi.org/10.1175/1520-0485\(1998\)028<1832:OTOSLS>2.0.CO;2](https://doi.org/10.1175/1520-0485(1998)028<1832:OTOSLS>2.0.CO;2)
- Trenberth, K. E., & Caron, J. M. (2001). Estimates of meridional atmosphere and ocean heat transports. *Journal of Climate*, *14*(16), 3433–3443. [https://doi.org/10.1175/1520-0442\(2001\)014<3433:EOMAAO>2.0.CO;2](https://doi.org/10.1175/1520-0442(2001)014<3433:EOMAAO>2.0.CO;2)
- Tripati, A. K., Delaney, M. L., Zachos, J. C., Anderson, L. D., Kelly, D. C., & Elderfield, H. (2003). Tropical sea-surface temperature reconstruction for the early Paleogene using Mg/Ca ratios of planktonic foraminifera. *Paleoceanography*, *18*(4), 1101. <https://doi.org/10.1029/2003PA000937>
- van Sebille, E., Griffies, S. M., Abernathy, R., Adams, T. P., Berloff, P., Biastoch, A., et al. (2018). Lagrangian ocean analysis: Fundamentals and practices. *Ocean Modelling*, *121*, 49–75. <https://doi.org/10.1016/j.ocemod.2017.11.008>
- van Sebille, E., Spence, P., Mazloff, M. R., England, M. H., Rintoul, S. R., & Saenko, O. A. (2013). Abyssal connections of Antarctic Bottom Water in a Southern Ocean state estimate: AABW pathways in SOSE. *Geophysical Research Letters*, *40*, 2177–2182. <https://doi.org/10.1002/grl.50483>
- Volkov, D. L., Fu, L.-L., & Lee, T. (2010). Mechanisms of the meridional heat transport in the Southern Ocean. *Ocean Dynamics*, *60*(4), 791–801. <https://doi.org/10.1007/s10236-010-0288-0>
- Watson, A. J., & Naveira Garabato, A. C. (2006). The role of Southern Ocean mixing and upwelling in glacial-interglacial atmospheric CO₂ change. *Tellus B: Chemical and Physical Meteorology*, *58*(1), 73–87. <https://doi.org/10.1111/j.1600-0889.2005.00167.x>
- Wolfe, C. L., & Cessi, P. (2011). The adiabatic pole-to-pole overturning circulation. *Journal of Physical Oceanography*, *41*(9), 1795–1810. <https://doi.org/10.1175/2011JPO4570.1>
- Wolfe, C. L., & Cessi, P. (2014). Salt feedback in the adiabatic overturning circulation. *Journal of Physical Oceanography*, *44*(4), 1175–1194. <https://doi.org/10.1175/JPO-D-13-0154.1>
- Zhang, Y., Huck, T., Lique, C., Donnadieu, Y., Ladant, J.-B., Rabineau, M., & Aslanian, D. (2020). Early Eocene vigorous ocean overturning and its contribution to a warm Southern Ocean. *Climate of Past*, *16*, 1263–1283. <https://doi.org/10.5194/cp-16-1263-2020>